MNRAS **000**, 1–25 (2015) Preprint 26 January 2016 Compiled using MNRAS LATEX style file v3.0

The SAMI Galaxy Survey: extraplanar gas, galactic winds, and their association with star formation history

I-Ting Ho (何宜庭)[1,2⋆], Anne M. Medling[2], Joss Bland-Hawthorn[3], Brent Groves[2], Lisa J. Kewley[1,2], Chiaki Kobayashi[4], Michael A. Dopita[2,5], Sarah K. Leslie[2], Rob Sharp[2,6], James T. Allen[3,6], Nathan Bourne[7], Julia J. Bryant[3,6,8], Luca Cortese[9,10], Scott M. Croom[3,6], Loretta Dunne[7], L. M. R. Fogarty[3,6], Michael Goodwin[8], Andy W. Green[8], Iraklis S. Konstantopoulos[8,11], Jon S. Lawrence[8], Nuria P. F. Lorente[8], Matt S. Owers[8,12], Samuel Richards[3,6,8], Sarah M. Sweet[2], Edoardo Tescari[6,13] and Elisabetta Valiante[14]

[1] *Institute for Astronomy, University of Hawaii, 2680 Woodlawn Drive, Honolulu, HI 96822, USA*
[2] *Research School of Astronomy and Astrophysics, Australian National University, Canberra, ACT 2611, Australia*
[3] *Sydney Institute for Astronomy, School of Physics, University of Sydney, NSW 2006, Australia*
[4] *Centre for Astrophysics Research, Science and Technology Research Institute, University of Hertfordshire, Hertfordshire AL10 9AB, UK*
[5] *Astronomy Department, King Abdulaziz University, P.O. Box 80203, Jeddah, Saudi Arabia*
[6] *ARC Centre of Excellence for All-sky Astrophysics (CAASTRO)*
[7] *Institute for Astronomy, University of Edinburgh, Royal Observatory, Blackford Hill, Edinburgh, EH9 3HJ, UK*
[8] *Australian Astronomical Observatory, PO Box 915, North Ryde, NSW 1670, Australia*
[9] *Centre for Astrophysics & Supercomputing, Swinburne University of Technology, Victoria, Australia*
[10] *International Centre for Radio Astronomy Research, University of Western Australia, 35 Stirling Highway, Crawley, WA 6009, Australia*
[11] *Envizi Group Suite 213, National Innovation Centre, Australian Technology Park, 4 Cornwallis Street, Eveleigh, NSW 2015, Australia*
[12] *Department of Physics and Astronomy, Macquarie University, NSW 2109, Australia*
[13] *School of Physics, University of Melbourne, Parkville, VIC 3010, Australia*
[14] *School of Physics and Astronomy, Cardiff University, Queen's Buildings, Cardiff, CF24 3AA, UK*

arXiv:1601.02022v2 [astro-ph.GA] 23 Jan 2016

Accepted 2016 January 04. Received 2016 January 03; in original form 2015 September 22

ABSTRACT

We investigate a sample of 40 local, main-sequence, edge-on disc galaxies using integral field spectroscopy with the Sydney-AAO Multi-object Integral field spectrograph (SAMI) Galaxy Survey to understand the link between properties of the extraplanar gas and their host galaxies. The kinematics properties of the extraplanar gas, including velocity asymmetries and increased dispersion, are used to differentiate galaxies hosting large-scale galactic winds from those dominated by the extended diffuse ionized gas. We find rather that a spectrum of diffuse gas-dominated to wind dominated galaxies exist. The wind-dominated galaxies span a wide range of star formation rates ($-1 \lesssim \log(\mathrm{SFR/M_\odot yr^{-1}}) \lesssim 0.5$) across the whole stellar mass range of the sample ($8.5 \lesssim \log(\mathrm{M_*/M_\odot}) \lesssim 11$). The wind galaxies also span a wide range in SFR surface densities (10^{-3}–$10^{-1.5}$ $\mathrm{M_\odot\ yr^{-1}\ kpc^{-2}}$) that is much lower than the canonical threshold of 0.1 $\mathrm{M_\odot\ yr^{-1}\ kpc^{-2}}$. The wind galaxies on average have higher SFR surface densities and higher $\mathrm{H}\delta_\mathrm{A}$ values than those without strong wind signatures. The enhanced $\mathrm{H}\delta_\mathrm{A}$ indicates that bursts of star formation in the recent past are necessary for driving large-scale galactic winds. We demonstrate with Sloan Digital Sky Survey data that galaxies with high SFR surface density have experienced bursts of star formation in the recent past. Our results imply that the galactic winds revealed in our study are indeed driven by bursts of star formation, and thus probing star formation in the time domain is crucial for finding and understanding galactic winds.

Key words: galaxies: evolution – galaxies: starburst – galaxies: kinematics – galaxies: ISM

© 2015 The Authors
⋆ E-mail: itho@ifa.hawaii.edu

1 INTRODUCTION

In the standard picture of galaxy formation and evolution, the feedback related to processes that drive energy and momentum into the interstellar gas serve to regulate the assembly of baryonic matter in dark matter haloes. Outflows from galaxies prevent further gas accretion and eject gas, metals, and energy out to many kpc into their haloes. The overy of large amounts of gas, metals, and, dust in the circumgalactic medium (at a few hundred kpc radius) has established the important role that this halo matter must play in galaxy evolution (Ménard et al. 2010; Tumlinson et al. 2011; Werk et al. 2013, 2014; Peek et al. 2015). The halo gas may eventually cool down and fall back to the disc to feed subsequent star formation (i.e. the "galactic fountain" picture; Shapiro & Field 1976; Bregman 1980; de Avillez 2000), or it may be lost to the system through interactions with other galaxies. The interplay between the discs and their haloes can strongly influence the different pathways galaxies evolve upon over cosmic time.

Star formation and active galactic nuclei (AGN) are the two major energy sources capable of ejecting baryonic matter from the disc into the halo. Different energy input rates and their time-scales dictate the form of interactions between galaxies and their haloes.

At the very energetic end, powerful AGNs can deposit energy and momentum from small to large scales, ejecting multiphase gas at velocities of more than a thousand kilometres per second (e.g. Tremonti et al. 2007; Rupke & Veilleux 2013; Veilleux et al. 2013). At intermediate energy, galactic winds driven by star formation can typically reach a speed of a few hundred kilometres per second and are known to be very common at high redshifts ($z > 1$) where the cosmic star formation rates (SFRs) are high (e.g. Weiner et al. 2009; Steidel et al. 2010). In the local Universe, starburst-driven winds are ubiquitous in galaxies with high enough SFR surface densities ($\Sigma > 0.1 M_{\odot}$ yr^{-1} kpc^{-2}; Heckman 2002). Although present-day normal galaxies do not have such high SFR surface densities, the prevalence of galactic winds is still implied statistically by stacking analysis with the Na D absorption lines (Chen et al. 2010). At intermediate redshifts ($0.3 < z < 1$), the ubiquity of galactic-scale outflows has also been inferred by absorption line studies in individual systems using 10-m class telescopes (e.g. Rubin et al. 2014; Schroetter et al. 2015; see also Sato et al. 2009; Martin et al. 2012; Kornei et al. 2012). Finally at low energy, the extended diffuse ionized gas (eDIG), as part of the warm ionized medium seen both in our Milky Way (also known as the Reynolds Layer; Reynolds et al. 1973) and external galaxies represents the interface between the hot haloes and the cold discs (see Haffner et al. 2009 for an extensive review).

The interactions between disc activities and haloes (the so-called "disc-halo interactions") can be effectively probed by study of the extraplanar emissions at the interface where the interactions occur. Edge-on galaxies provide the best viewing angle for the investigation of the structure, excitation, and dynamics of the extraplanar gas.

In nearby edge-on galaxies that host well-known starburst driven winds, such as M82 (Axon & Taylor 1978; Bland & Tully 1988; Leroy et al. 2015), NGC253 (Westmoquette et al. 2011), NGC3079 (Veilleux et al. 1994; Cecil et al. 2001, 2002) and NGC1482 (Veilleux & Rupke 2002), open-ended bipolar structures can extend several kpc from the central energy injection zones undergoing concentrated starbursts. Strong supernova feedback drives multiphase gas consisting of hot 10^{7-8} K X-ray emitting gas, warm 10^4 K ionized gas, and cold neutral atomic and molecular gas, to a speed of a few hundred kilometres per second (see Veilleux et al. 2005 for a review). The optical line-emitting gas usually presents well-defined conical structures, which are the limb-brightened parts of the expanding X-ray bubbles that also entrain the ambient cold gas. As the bubbles expand supersonically, shock waves excite optical emission lines and produce the characteristically large [O I], [O II], [N II] and [S II] to Balmer line ratios. This extraplanar gas in nearby prototype wind systems represents a very violent form of interactions between discs and haloes.

In galaxies lacking spectacular large-scale winds, narrowband Hα imaging in nearby late-type edge-on galaxies reveals that eDIG is very common, with more than half of the galaxies showing extraplanar diffuse emissions and sometimes filamentary structures (e.g. Rossa & Dettmar 2000, 2003a,b; Miller & Veilleux 2003a; Rossa et al. 2004). The average distances of the extended emission above the galactic midplane can range from 1–2 to 4 kpc or more. Kinematic studies suggest that the eDIG co-rotates with the host galaxy and usually presents a slight lag in the azimuthal velocity, which increases with increasing off-plane distance (Heald et al. 2006b,a, 2007). O-stars in H II regions are likely to contribute significantly to the excitation of eDIG (Miller & Cox 1993; Dove & Shull 1994). Escaping Lyman continuum photons from O-star H II regions travelling in a low density, fractal medium or superbubble chimney could reach kpc scales and excite the extraplanar gas. This picture naturally explains the observed correlations between the far infrared luminosity per unit area and extraplanar ionized mass (and also the presence of extraplanar emission Miller & Veilleux 2003a; Rossa & Dettmar 2003a). This picture also explains the strong spatial correlation between strong diffuse emission and H II regions in the disc (Zurita et al. 2000, 2002). However, Miller & Veilleux (2003b) modelled the forbidden line ([O III] $\lambda\lambda$4959,5007, [O I] λ6300, and [S II] $\lambda\lambda$6716,6731) to Balmer line ratios of the extended filaments which typically increase with increasing height off the disc plane (e.g. Otte et al. 2001, 2002). They found that in most cases photoionization is unlikely to be the only excitation mechanism, with hybrid models combining photoionization and turbulent mixing layers or shocks better explaining the optical line ratios (see also Reynolds et al. 1999; Collins & Rand 2001; Seon 2009; Barnes et al. 2014).

Understanding the underlying physical processes and galaxy properties that drive the different types of disc-halo interactions is critical for building a more comprehensive picture of the cycle of baryonic matter in galaxy evolution. Extraplanar gas can shed light on the different strengths and forms of the interactions. Observing such interactions in large numbers of galaxies has been made possible recently by virtue of the growth of integral field spectroscopy. The ongoing integral field spectroscopy (IFS) surveys, such as the the Calar Alto Legacy Integral Field Area Survey (CALIFA; Sánchez et al. 2012), the Sydney-AAO Multi-object Integral field spectrograph (SAMI) Survey (Croom et al. 2012; Bryant et al. 2015), and the Mapping Nearby Galaxies at

Apache Point Observatory (MaNGA) Survey (Bundy et al. 2015), are delivering three dimensional datacubes of hundreds to tens of thousands of galaxies and starting to revolutionize the way galaxies are studied. In this work, we will explore extraplanar emissions in edge-on discs using data from the SAMI Galaxy Survey and investigate the connection between properties of the extraplanar gas and physical properties of the galaxies.

The paper is structured as follows. Section 2 describes our sample selection. We uss the analysis of our IFS datacubes in Section 3, and introduce in Section 4 a novel approach of empirically identifying wind-dominated galaxies. In Section 5, we detail the derivation of host galaxy properties including star formation rate and star formation history. In Section 6, we investigate common physical properties of wind-dominated galaxies. Finally, we uss the implications of our results in Section 7 and provide a summary and conclusion in Section 8.

Through out this paper, we assume the concordance Λ cold dark matter cosmology with $H_0 = 70$ km s^{-1} Mpc^{-1}, $\Omega_{\rm M} = 0.3$ and $\Omega_\Lambda = 0.7$. We infer cosmological distances from redshifts that have been corrected for local and large-scale flows using the flow model by Tonry et al. (2000).

2 SAMPLE SELECTION

We select edge-on star-forming disc galaxies from the SAMI Galaxy Survey. The on-going SAMI Galaxy Survey observes low redshift galaxies ($z \approx 0.05$) using deployable imaging fiber bundles ("hexabundles") to obtain spatially-resolved optical spectra over a circular field of view (FOV) of 15 arcsec in diameter (Croom et al. 2012). The survey is conducted on the 3.9-m Anglo-Australian Telescope using the flexible AAOmega dual-beam spectrograph (Smith et al. 2004; Saunders et al. 2004; Sharp et al. 2006). For a comprehensive ussion of the sample selection, the reader is directed to the survey sample selection paper by Bryant et al. (2015). In brief, the SAMI sample is selected from the Galaxy And Mass Assembly project (GAMA; Driver et al. 2009) using stellar-mass cut-offs in redshift bins up to $z < 0.12$. The GAMA sample covers broad ranges in stellar mass and environment. SAMI also includes an addition of eight clusters to probe the higher density environments. Our edge-on discs are selected from the GAMA sample that contains about 830 galaxies at the present stage of the survey (June 2015).

We impose criteria on the galaxy inclination angles and effective radii to ensure that the selected galaxies are edge-on discs well-covered by the SAMI hexabundles. We require minor-to-major axis ratio (b/a) in the r-band to be less than 0.26, which corresponds to a lower limit on inclination angle of 80 degrees, assuming the classical Hubble formula[1] (Hubble 1926). We also require the r-band effective radii (r_e; or half-light radii) to be less than 12 arcsec, such that the SAMI hexabundles cover more than 50% of the total light for the majority of the sample. The effective radii were measured on Sloan Digital Sky Survey (SDSS; York et al. 2000) r-band images by the GAMA team using GALFIT (Peng et al. 2010; Kelvin et al. 2012). We reject major mergers showing clear tidal features because their complex large-scale winds are not the subject of this study (e.g. Wild et al. 2014). These geometrical and morphological selection criteria yield 82 galaxies. From this sample, we further reject AGNs as those galaxies whose line ratios [N II] λ6583/Hα and [O III] λ5007/Hβ at the central spaxels are below the theoretical maximum starburst line by Kewley et al. (2001). Galaxies lacking enough spaxels outside $1r_e$ detected in Hα are also not considered because their data do not yield strong constraints on the extraplanar gas properties (see Section 4). These galaxies

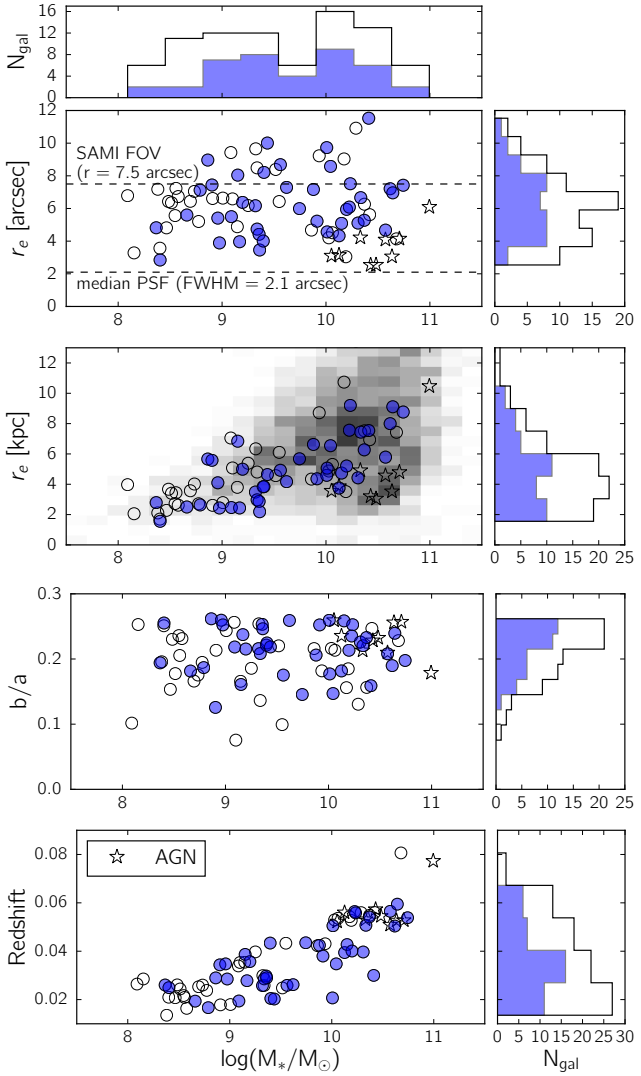

Figure 1. Distributions of our galaxies in stellar mass, r-band effective radius, minor-to-major axis ratio, and redshift. The circles and stars are the 82 galaxies that satisfy our geometrical (inclination angle $>$ 80 degrees [$b/a < 0.26$] and $r_e < 12$ arcsec) and morphological (not major merger) selections. The open circles are galaxies lacking sufficient Hα detections outside $1r_e$ (N$_{\rm gal}$ = 33) and the open stars are AGNs (N$_{\rm gal}$ = 9). These galaxies are excluded from this work. Our final sample corresponds to the filled blue circles (N$_{\rm gal}$ = 40). The blue and black histograms are the distributions for our final sample and all the 82 galaxies, respectively. Grey scale in the r_e [kpc] versus stellar mass panel shows the mass-size relation of galaxies in the GAMA survey with inclination angles $>$ 80 degrees ($b/a < 0.26$).

[1] $\cos^2 i = \frac{(b/a)^2 - q_0^2}{1 - q_0^2}$, where i is the inclination angle and q_0 is a constant of 0.2 ($i = 90°$ for $b/a < q_0$).

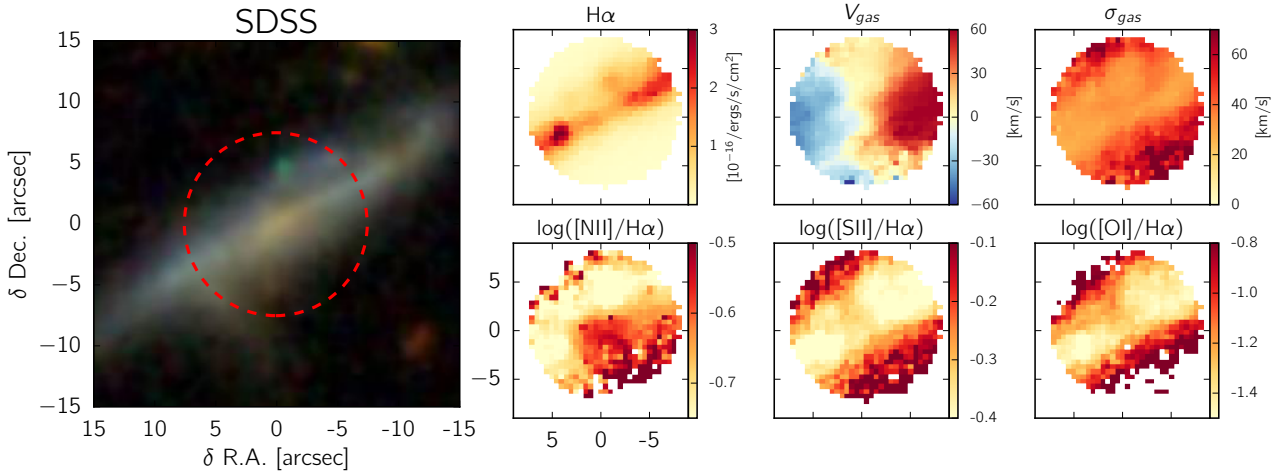

Figure 2. Examples of 2D maps reconstructed from the IFS datacubes of GAMAJ115927.23-010918.4 (CATAID: 31452). The dashed red circle in the SDSS 3-colour image (right panel) shows approximately the FOV and pointing of SAMI (15 arcsec in diameter). Note the increase in velocity dispersion and line ratios off the disc plane and the disturbed velocity field are all indicative of galactic winds. We adopt S/N cuts of 3 in these maps. North is up and east is left.

without good detections on average have lower star formation rates and lower star formation surface densities than those with good detections. After imposing these two criteria, we work with 40 galaxies, representing approximately 5% of the current SAMI GAMA sample.

Figure 1 shows the stellar mass, redshift, b/a, and r_e distributions of our sample. The filled circles are our final sample ($N_{gal} = 40$). The open symbols (circles and stars) are those satisfying our geometric and morphological selections but either have insufficient detections of extraplanar emissions ($N_{gal} = 33$) or are AGN hosts (open stars; $N_{gal} = 9$). We adopt the photometrically-derived stellar masses from the GAMA survey (Taylor et al. 2011). The strong correlation between redshift and stellar mass is a direct result of the selection function of SAMI (see Bryant et al. 2015 for details). The lack of correlation between r_e in arcsec and stellar mass suggests that our resolution normalized to galaxy size is on average the same for galaxies of different masses .

3 DATA ANALYSIS

3.1 Data reduction

The integral field spectroscopic data are reduced using the automatic data reduction pipeline described in Sharp et al. (2015) and Allen et al. (2015). We first reduce the spectrum of each fiber following the standard data processing procedures for optical spectroscopy using the 2DFDR[2] data reduction pipeline (Croom et al. 2004), and subsequently resample the spectra on to a rectangular grid of 0.5 arcsec using the drizzle technique (Fruchter & Hook 2002; Sharp et al. 2015). The reduced data products comprise two datacubes for every galaxy, one for each of the red and blue arms. The blue datacube covers ≈ 3750–5800Å with a spectral sampling of 1.04Å and spectral resolution of R ≈ 1750 or full-width at half-maximum (FWHM) of ≈ 170 km s^{-1}. The red datacube covers ≈ 6300–7425Å with a spectral sampling of 0.57Å and spectral resolution of R ≈ 4500 or FWHM ≈ 65 km s^{-1}. The angular resolution of the data is in the range of 1.4 – 3.0 arcsec, with a median value of 2.1 arcsec. The median angular resolution corresponds to about 0.8 to 2.8 kpc at the distances of our sample.

3.2 Emission line fitting

We apply spectral fitting to extract emission line fluxes and kinematic information from the datacubes. Our emission line fitting toolkit LZIFU (Ho et al. in preparation; see also Ho et al. 2014) is employed to construct 2-dimensional maps. LZIFU adopts the penalized pixel-fitting routine (PPXF; Cappellari & Emsellem 2004) to model (and subsequently subtract) the stellar continuum and the Levenberg-Marquardt least-squares method (Markwardt 2009) to fit Gaussian profiles to the user-assigned emission lines. For fitting the stellar continuum, we adopt the theoretical simple stellar population (SSP) models assuming Padova isochrones of 24 ages[3] and 3 metallicities[4] from González Delgado et al. (2005). We model 11 emission lines simultaneously as simple Gaussians requiring them to share the same velocity and velocity dispersion. The 11 emission lines are [O II] λλ3726,3729, Hβ, [O III] λλ4959,5007, [O I] λ6300, [N II] λλ6548,6583, Hα, and [S II] λλ6716,6731. We fix the ratios [O III] λλ4959/5007 and [N II] λλ6548/6583 to their theoretical values given by quantum mechanics. Hereafter, we omit the wavelength notation when appropriate, i.e., [O III]≡ [O III] λ5007, [N II]≡ [N II] λ6583, [O I]≡ [O I] λ6300, and [S II]≡ [S II] λλ6716,6731

[2] http://www.aao.gov.au/science/software/2dfdr

[3] equally spaced on a logarithmic scale between 0.004 and 11.220 Gyr

[4] Z = 0.004, 0.008, and 0.019

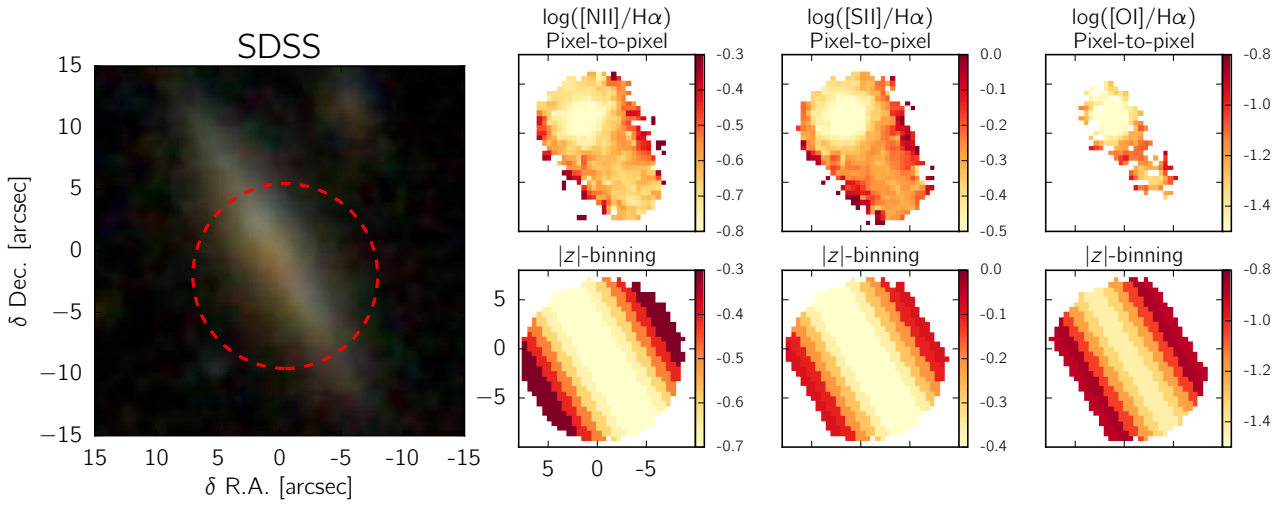

Figure 3. Examples of 2D line ratio maps reconstructed from the IFS datacubes of GAMAJ120221.91-012714.1 (CATAID: 185510). The SAMI FOV and pointing position are shown as the red dashed circle in the SDSS 3-colour image (right panel). We create the line ratio maps in two different methods: pixel-to-pixel (upper panels) and adaptive $|z|$-binning (lower panels; see Section 3.2). The adaptive $|z|$-binning bins symmetrically on either side of the disc. The $|z|$-binning maps trace the emission line ratios of the ionized gas unambiguously out to larger $|z|$ than the pixel-to-pixel maps. We adopt S/N cuts of 5 in these maps.

3.2.1 Pixel-to-pixel maps

Figure 2 shows the emission line flux, line ratio, and kinematic maps of GAMA J115927.23-010918.4 (CATAID[5]: 31452) and demonstrates the immediate products coming out of our LZIFU pipeline. These maps are useful for investigating the properties of the extraplanar gas, as we will elaborate on in later sections. In this particular galaxy, several features are immediately obvious and imply the presence of large-scale galactic winds. The [N II]/Hα, [S II]/Hα and [O I]/Hα line ratio maps show that the line ratios increase as a function of height off the disc plane, and suggest that the physical conditions of the ionized gas change dramatically off the disc plane. The enhanced line ratios are likely due to shocks embedded in galactic winds. The gas in partially ionized, post-shock regions emits strong forbidden lines from low ionization species and hydrogen recombination lines (Allen et al. 2008). The elevated velocity dispersion seen in the σ_{gas} map is also consistent with the broad kinematic component seen in IFS data of other wind galaxies (e.g. Rich et al. 2010, 2011; Fogarty et al. 2012; Ho et al. 2014). Two additional interesting features stand out from these maps. In the [N II]/Hα map, an elevated [N II]/Hα cone-shaped region pointing south-west could be tracing an ionization cone emerging from the energy injection zone at the centre of the galaxy. We do not observe the other side of the putative bipolar structure presumably due to dust obscuration or intrinsic asymmetry of the winds. This feature is very similar to the bipolar structures that have been observed in the nearby starburst galaxies NGC 253 (Westmoquette et al. 2011) and NGC3079 (Cecil et al. 2001). The velocity map of the gas, v_{gas}, shows that the overall velocity gradient is mis-aligned with the galaxy disc, which is caused by the complex velocity field of the bipolar winds superimposed on the disc rotation (see Section 4). Although there are no strong indications of on-going interactions in GAMA J115927.23-010918.4 (z = 0.0202), the presence of nearby galaxy GAMA J115923.94-010915.4 (about 50 arcsec or 23 kpc away) at a similar redshift (z = 0.0204) implies that the environment might play a role in triggering the winds (e.g. Rich et al. 2010; Vogt et al. 2013). Higher spatial resolution and multi-wavelength observations are required to determine the precise geometry and cause of the galactic winds in GAMA J115927.23-010918.4; nevertheless, the pixel-to-pixel maps reconstructed from our IFS data are sufficient to reveal the existence of strong disc-halo interactions through galactic winds.

3.2.2 Adaptive $|z|$-binning

GAMA J115927.23-010918.4 in Figure 2 is one of the best cases in our sample where clear wind signatures are detected. However, since extraplanar line emission is typically much fainter than that of the disc, we spatially bin the datacube parallel to the disc plane ($|z|$-binning). This improves our detection limits at the cost of losing some spatial and kinematic information of the extraplanar gas.

In the analysis we adopt "adaptive $|z|$-binning" to ensure adequate signal-to-noise ratio (S/N) in the following way. First, we produce a bin reference map where the SAMI FOV is divided into 1-arcsec wide slices parallel to the disc (half the typical spatial resolution). We then bin together the required number of slices *symmetrically* until the S/N of [S II] λ6716 reaches 5. Close to the plane of the disc, the S/N may be already sufficient, leading to a bin containing only the first 1-arcsec-wide slice above and below the disc plane. As flux drops off at larger distances from the disc plane, we adopt larger bins to obtain the required S/N (i.e. containing several matched slices from above and below the disc). This symmetric binning assumes that the ionized gas above and below the disc share the same physical properties. Spaxels

[5] CATAID is the galaxy identifier of GAMA

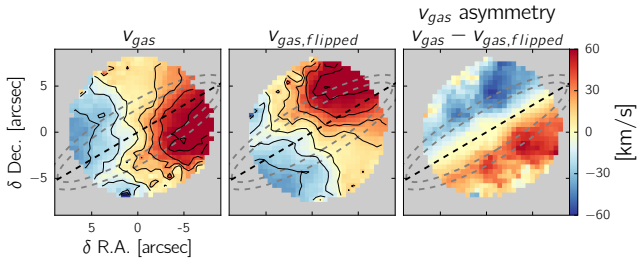

Figure 4. The velocity asymmetry across the major axis of GAMAJ115927.23-010918.4 (CATAID: 31452 ; Figure 2). The middle panel ($v_{gas,flipped}$) is the velocity field (v_{gas}) in the left panel flipped over the galaxy major axis. The difference between the left and middle panels is shown in the right panel ($v_{gas} - v_{gas,flipped}$, or the velocity residual map). Contours are equally spaced in 15km s^{-1} intervals. The dashed black line indicates the major axis of the galaxy. The grey dashed circles indicate concentric ellipses of $1r_e$ (inner) and $1\tilde{r}_e$ (outer) centered at the galaxy optical centre. The outer ellipses are approximately 1 arcsec larger than the inner ellipses. The strong residuals outside $1\tilde{r}_e$ are clear signs of galactic winds.

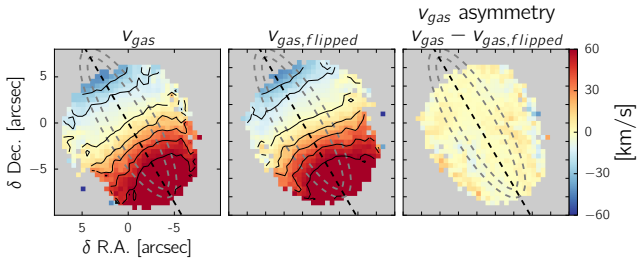

Figure 5. Same as Figure 4 but for GAMAJ120221.91-012714.1 (CATAID: 185510 ; Figure 3). The small residuals in the right panel and the line ratio gradients in Figure 3 imply the presence of eDIG.

inside the final bins are summed and the binned spectra are re-analysed by LZIFU.

As a technical note, we take into account non-zero covariance between neighbouring spaxels while binning the datacubes. The cubing algorithm in our data reduction pipeline resamples the observed row stacked spectra of multiple dithers on to a rectangular grid, which results in correlated noise between neighbouring spaxels (see Sharp et al. 2015 and Allen et al. 2015). The appropriate way to preserve the variance when binning the data is to bin the datacubes and refit the binned spectra, rather than binning the pixel-to-pixel emission line maps.

In Figure 3, we show examples of some line ratio maps from fitting the un-binned datacubes and binned datacubes of GAMA J120221.91-012714.1 (CATAID: 185510). Spaxels or spatial bins with S/N< 5 on any of the lines associated with the relevant line ratios are masked out. Figure 3 demonstrates the advantage of the adaptive $|z|$-binning approach over the traditional pixel-to-pixel approach. The $|z|$-binning maps can trace the ionized gas unambiguously out to larger $|z|$ while single spaxels at such large distances may not survive the S/N cuts and thus provide less of a constraint on the physical conditions of the gas.

4 GAS KINEMATICS

While optical line ratios shed light on the underlying excitation sources of the extraplanar gas, the velocity and velocity dispersion of the gas provide additional constraints on the form and strength of disc-halo interactions.

4.1 Asymmetry of the extraplanar velocity field

We empirically quantify the strength of disc-halo interactions by the regularity and (a)symmetry of the velocity field. In the cases of weak (or no) disc-halo interactions (e.g. eDIG with no gas flows), the extraplanar gas co-rotates with the disc and usually presents a slight lag in the azimuthal velocity. A vertical gradient in azimuthal velocity of approximately 10 to 30 km s^{-1} kpc^{-1} has been found in nearby galaxies where high quality optical or H I data are available (e.g. Fraternali et al. 2005; Heald et al. 2006b,a, 2007; Zschaechner et al. 2015). There is no strong evidence of pronounced asymmetry in the vertical gradient, i.e. the gas above and below the disc slows down equally with $|z|$; however, data of high enough quality to constrain the levels of asymmetry remain scarce. In the case of strong disc-halo interactions through galactic winds, the bipolar outflows commonly present opposite velocity fields on either side of the disc. The flow axis is approximately perpendicular to the disc plane but even in extreme edge-on systems the outflow velocity fields are never perfectly symmetric across the major axes of the hosts (e.g. Shopbell & Bland-Hawthorn 1998; Cecil et al. 2001; Sharp & Bland-Hawthorn 2010; Westmoquette et al. 2011). The asymmetry of the velocity fields is presumably due to a combination of the outflow axis not lying exactly on the plane of the sky, the clumpy, dusty interstellar medium, the highly structural nature of the wind filaments, and the wide opening angle of the bipolar cones (typically 40 to 60 degrees).

Thus, to determine whether the extraplanar emissions trace winds or eDIG, we quantify the velocity asymmetry across the galaxy major axis on the velocity map. We first flip the pixel-to-pixel velocity map over the galaxy major axis, $v_{gas,flipped}$, and subtract the flipped map from the original map (Figures 4 and 5). We define an "asymmetry parameter", ξ, that quantifies the flatness of $v_{gas} - v_{gas,flipped}$ (i.e. the velocity asymmetry map):

$$\xi = \frac{\tilde{\xi}_+ + \tilde{\xi}_-}{2}, \quad (1)$$

where

$$\tilde{\xi}_{+/-} = \underset{r_{+/-} > \tilde{r}_e}{\text{std}} \left(\frac{v_{gas} - v_{gas,flipped}}{\sqrt{Err(v_{gas})^2 + Err(v_{gas,flipped})^2}} \right). \quad (2)$$

Here, $Err(v_{gas})$ is the 1σ map from LZIFU, and $Err(v_{gas,flipped})$ is the corresponding map for $v_{gas,flipped}$. The ξ parameter measures the standard deviation of the S/N of the velocity asymmetry map (i.e. residuals) using only pixels outside the elliptical aperture of $\tilde{r}_e$[6]. This characteristic radius $\tilde{r}_e$ is the r-band effective radius increased by

[6] We define the optical centre in our IFS data using the continuum image summed over the red datacube. We fit a Sérsic profile using GALFIT to the IFS continuum image while fixing the shape parameters to those determined from the GAMA team fit to the SDSS r-band image.

approximately 1 arcsec to reduce the effect of beam smearing. Only spaxels with S/N(Hα) > 5 are considered, and all 40 of our galaxies have more than 150 spaxels outside $\tilde{r}_e$. We adopt the mean value of the standard deviations on either side of the disc (i.e. $\tilde{\xi}_+$ and $\tilde{\xi}_-$) as ξ[7]. As a technical note, to obtain the flipped maps, we first reflect the pixel centres over the galaxy major axis and then linearly interpolate the v_{gas} and $Err(v_{gas})$ maps around the reflected positions.

A perfectly symmetric velocity field would yield ξ of roughly unity as a result of random noise fluctuation in the velocity asymmetry map. The asymmetry parameter ξ becomes much larger than unity when the velocity asymmetry map is not flat due to asymmetry in the velocity field.

Figure 4 illustrates our methodology applied to the galaxy in Figure 2, which has the largest ξ in our sample (ξ = 11.9). The strong residuals outside $1\tilde{r}_e$ are clear evidence of galactic winds, consistent with the line ratio, structural, and kinematic signatures seen in Figure 2. The flat residuals inside $1\tilde{r}_e$ indicate the good symmetry of the prominent disc rotation. Figure 5 shows the same application on the galaxy in Figure 3. No strong residuals are visible on the velocity asymmetry map ($v_{gas} - v_{gas,flipped}$; ξ = 1.3) despite the clear line ratio gradients seen in Figure 3, implying the presence of eDIG rather than shocked outflowing gas. These sets of figures demonstrate the importance of using both kinematics and line ratios to investigate galactic winds and eDIG .

The parameter ξ can be used to trace winds or eDIG under the assumptions that our edge-on discs are regular and not heavily warped. Mergers are excluded from our sample (Section 2), and all our galaxies present regular rotation on their discs, consistent with not undergoing major interactions (see below Figures 7 and A1). The SDSS images also suggest that all the galaxies have regular discs without strong warp signatures. Although warping of stellar discs is common, the warps are only important at large radii (3–6 times the disc scalelength or 2–4r_e; Saha et al. 2009), typically beyond the SAMI FOV for the majority of our sample (90%). Thus, our velocity asymmetry parameter predominately reflects how the extraplanar gas is effected by winds.

It is worth pointing out that our approach of quantifying velocity asymmetry does not depend on any kinematic modeling, which can be non-trivial due to the edge-on viewing angle. Future work should develop 3-dimensional models that include the effects of beam smearing (such as the approach by Józsa et al. 2007 and Di Teodoro & Fraternali 2015) and radiative transfer to reproduce the emission line data cubes.

4.2 Elevated extraplanar velocity dispersion

We also make use of the velocity dispersion of the extraplanar gas to assess the form and strength of disc-halo interactions. In the case of weak (or no) interactions, the velocity dispersion of eDIG arises predominately from line-of-sight projection of the gas corotation with the disc. Heald et al. (2006b,a, 2007) found extraplanar $\sigma_{gas} \lesssim 50$ km s^{-1} in NGC 891, NGC 5775, and NGC 4302. These three edge-on discs have very similar ionized gas rotation velocities ($v_{rot} \approx$ 170–200 km s^{-1}) and stellar masses ($\log(M_*/M_\odot) \approx 10.7$). Their findings imply that $\sigma_{gas}/v_{rot} \lesssim 0.3$ for eDIG. In the case of strong interactions, the velocity dispersion of the extraplanar gas is broadened by both the turbulent motion of the outflowing gas and line splitting caused by emissions from the approaching and receding sides of the outflow cones. The magnitude of the line splitting depends on outflow velocities, topology and inclination angle. In classical wind galaxies, line splitting of about 100 km s^{-1} is common (e.g. Heckman et al. 1990; Sharp & Bland-Hawthorn 2010). In the extreme case of M82, line splitting as high as 300 km s^{-1}can be easily resolved by optical spectrographs (Axon & Taylor 1978; Shopbell & Bland-Hawthorn 1998). A very broad component (FWHM of 300 km s^{-1}) from the halo gas has also been observed in M82 (Bland & Tully 1988). In less extreme winds, the line splitting could be too narrow for SAMI to resolve, especially if viewing the outflow cones from the side where the projected velocities are small. In fact, we do not see clear indications of line splitting in the majority of our wind candidates given the S/N of our data. Nevertheless, the increase in velocity dispersion as a result of unresolved line splitting is still strong evidence of the presence of outflows.

To quantify the extraplanar velocity dispersion, we invoke a simple parameter η_{50}, the "velocity dispersion to rotation ratio" parameter, defined as

$$\eta_{50} = \sigma_{50}/v_{rot}, \quad (3)$$

where σ_{50} is the median velocity dispersion of all spaxels outside $1\tilde{r}_e$ with S/N(Hα) > 5. As before, all 40 of our galaxies have more than 150 spaxels meeting our S/N criterion outside $1\tilde{r}_e$. The rotation velocity is measured on our velocity map from the spaxels along the optical major axis with the maximum velocity. This method is applied only when our FOV extends to $1.4r_e$ ($< R_{\rm SAMI} \approx 7.5$ arcsec). For an exponential disc, this radial distance corresponds to about 2.4 times the disc scale length at which typical rotation curves already reach their maximum velocities (Sofue & Rubin 2001; Cecil et al. 2015). For galaxies without sufficiently large spatial coverage, we use the stellar mass Tully-Fisher relation to infer v_{rot} (Bell & de Jong 2001). We note that for our purpose v_{rot} should ideally be the maximum rotation velocity of the ionized gas, and we approximate it using the Tully-Fisher relation. The stellar mass Tully-Fisher relation unfortunately exhibits a scatter of about 0.5 dex, which directly translates to a factor of 3 in the systematic uncertainty of η_{50}.

4.3 An empirical identification of wind-dominated galaxies

Based on the two different empirical parameters for quantifying the strength of disc-halo interactions, it should be possible to distinguish galactic winds from eDIG. Galactic winds are expected to show *both* high ξ and η_{50}, whereas eDIG has low ξ and η_{50}. That is, galactic winds both disturb the symmetry of the extraplanar velocity field and increase the extraplanar emission line widths, whereas eDIG should still follow the velocity field of the galaxy. If winds are the

[7] We note that $\tilde{\xi}_+$ and $\tilde{\xi}_-$ in principle contain redundant information but due to interpolation and finite grid size the two values are not exactly the same. We take the mean value to minimise such an artefact.

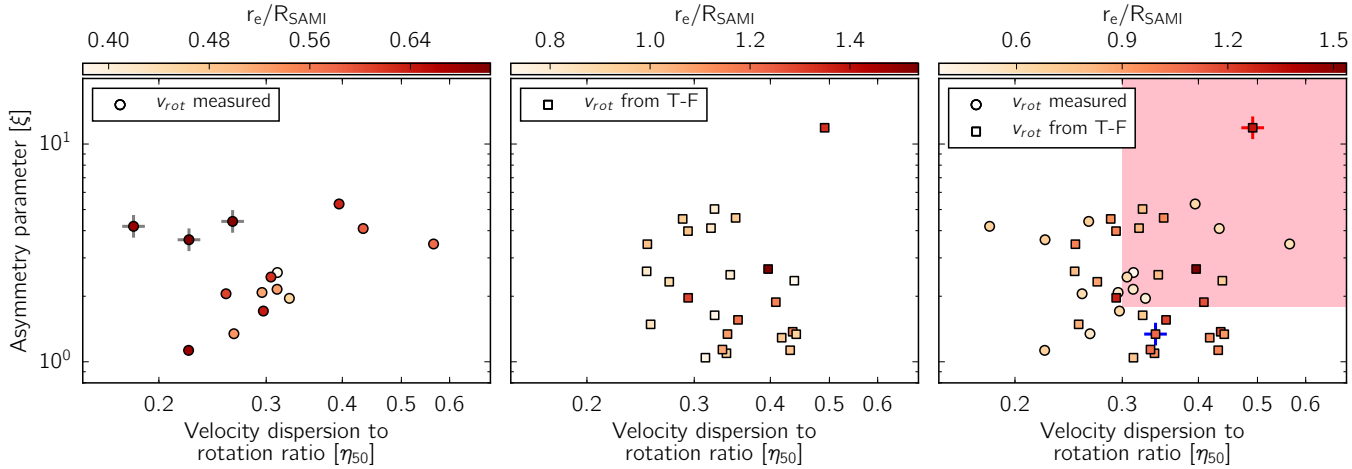

Figure 6. The asymmetry parameter of the velocity field ξ versus the velocity dispersion to rotation ratio parameter η_{50} of our sample. The left panel presents galaxies with v_{rot} measured from the SAMI data, the middle panel presents galaxies with v_{rot} inferred from the Tully-Fisher relation, and the right panel shows all the galaxies. The three high-ξ low-η_{50} galaxies marked by the grey crosses are ussed in Section 4.3. The red cross in the right panel corresponds to the example galaxy shown in Figures 2 and 4; and the blue cross in Figures 3 and 5. Galaxies falling in the shaded region in the right panel are identified as wind-dominated galaxies (see Figure 7).

only mechanism disrupting the extraplanar gas, then a trend between ξ and η_{50} is expected. Figure 6 shows our sample in the ξ versus η_{50} parameter space. We present separately galaxies with v_{rot} measured (left panel) and v_{rot} inferred from the Tully-Fisher relation (middle panel).

For galaxies with directly measured v_{rot}, it is inconclusive whether there is a trend between ξ and η_{50}. There are no galaxies in the lower right corner ($\eta_{50} \gtrsim 0.4$ and $\xi \lesssim 3$), however, there are three galaxies (marked with crosses) with larger ξ than the other galaxies of similar η_{50}. The Spearman rank correlation test implies no significant correlation for the galaxies in the left panel (ρ of 0.21 and p-value of 0.46), unless the three high-ξ low-η_{50} galaxies are excluded from the test (ρ of 0.80 and p-value of 0.0016). We speculate that there might be additional mechanisms responsible for causing the asymmetry of the extraplanar gas (see Section 7.3). A trend between ξ and η_{50} can not be confirmed by our medium-sized sample.

For galaxies with v_{rot} inferred from the Tully-Fisher relation, there is also no clear relationship between ξ and η_{50} and the Spearman rank correlation test suggests no significant correlation (ρ of -0.19 and p-value of 0.35). The lack of correlation is expected given that the scatter of Tully-Fisher relation (0.5 dex) yields a factor of 3 in the systematic uncertainty of η_{50}.

We conservatively select galaxies whose extraplanar gas is affected by galactic winds from the upper right corner of Figure 6. We select galaxies with $\eta_{50} > 0.3$ and $\xi > 1.8$, as defined by the shaded region in the right panel. These criteria yield 15 galaxies. For the purpose of presentation, we will henceforth refer these galaxies as "wind-dominated galaxies". Figure 7 presents their velocity, velocity asymmetry, velocity dispersion, and [S II]/Hα line ratio maps. The remaining galaxies are presented in the appendix (Figure A1). We note that it is, to some extent, unphysical to impose hard limits to identify wind galaxies. The distribution of our galaxies in the ξ versus η_{50} parameter space does not favour the idea that there exists distinct groups of galaxies with similar kinematic properties of their extraplanar gas; instead, the distribution could imply a continuous "strength sequence" of disc-halo interaction, connecting the very quiescent, non-interacting (or weakly interacting) eDIG to the very violent, strongly interacting classical galactic winds. It is likely that in galaxies not classified as wind-dominated, there could still be localized feedback from H II regions driving gas away from the discs, disturbing the extraplanar gas kinematics at small scales, and causing a slight increase in ξ and/or η_{50}. In fact, some galaxies (e.g. CATAID: 496966, 228066, 348116, 517594, 595027; Figure A1) indeed show indications of localised velocity asymmetry possibly driven by off-centre starbursts, consistent with the galactic chimney picture (Norman & Ikeuchi 1989). It is also likely that in some of the wind-dominated galaxies, a portion of the pre-existing eDIG remains co-rotating with the discs while the outflowing gas interacts with the rest of the eDIG. Given our sample size, it is nonetheless convenient to invoke a binary classification scheme in order to investigate the underlying physical processes governing the strength of disc-halo interactions.

The wind-dominated galaxies in Figure 7, by selection, show strong velocity asymmetry and elevated extraplanar velocity dispersion. Classical galactic wind signatures can be easily identified in these maps. Some galaxies (e.g. CATAID: 228432, 574200) present ionization cone signatures on their velocity dispersion maps and their velocity asymmetry maps, with strong velocity residuals tracing the limbs of the putative bipolar cones. In others (e.g. CATAID: 31452, 239249, 417678, 106389), the velocity asymmetry maps correlate spatially with the velocity dispersion maps and usually present positive/negative residuals on either sides of the discs. On the contrary, the remaining galaxies presented in the appendix do not show these kinematic signatures of galactic winds as clearly as the wind-dominated galaxies. In all the wind-dominated galaxies, the [S II]/Hα line ratio increases with $|z|$. This is partly due to excitation by shocks embedded in the outflows (see Section 6.2).

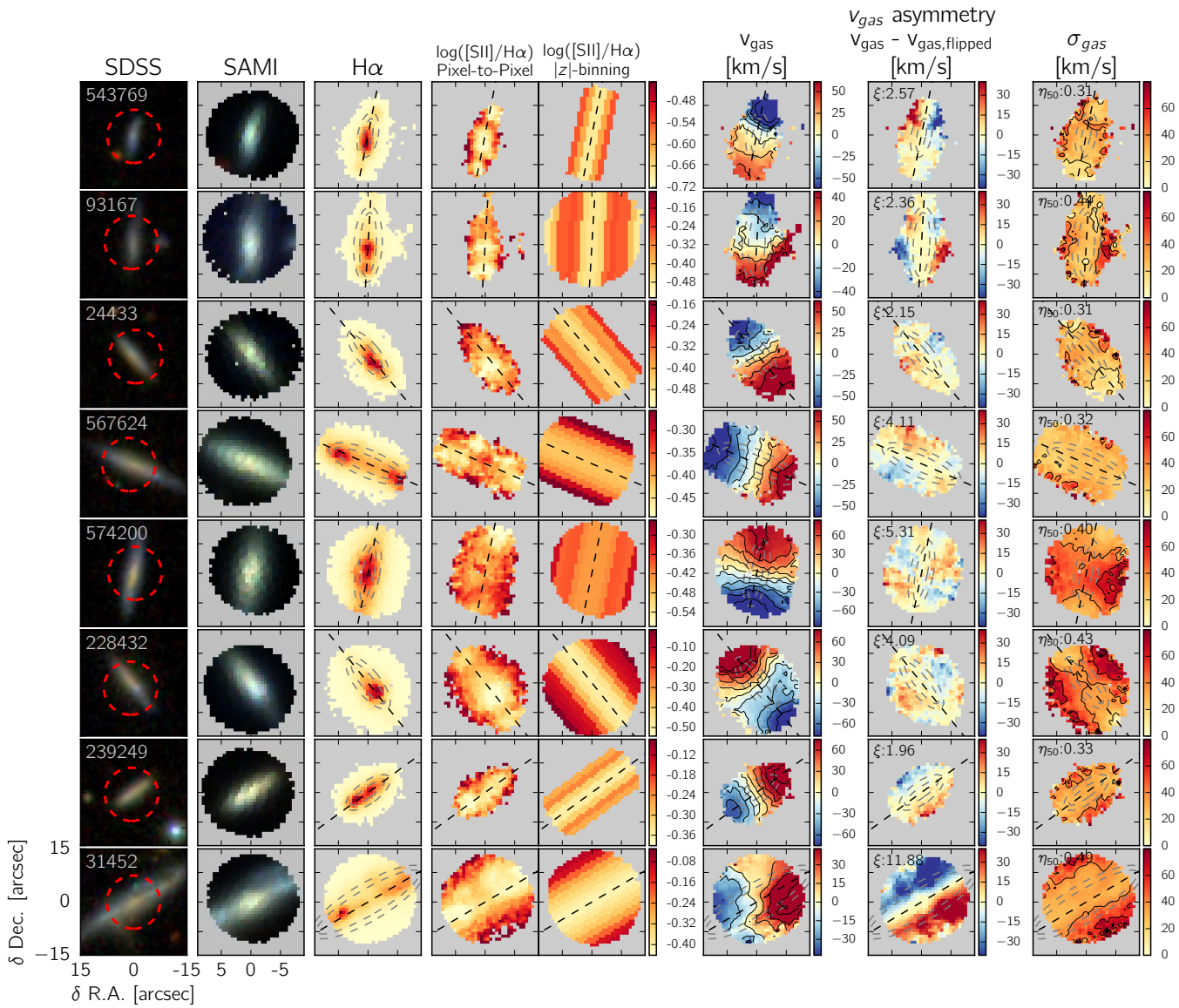

Figure 7. From left to right: SDSS 3-colour, SAMI 3-colour (red: 6300Å; green: 4800Å; blue: 4000Å), Hα, [S II]/Hα (pixel-to-pixel and adaptive $|z|$-binning), velocity, velocity asymmetry, and velocity dispersion maps of our wind-dominated galaxies ($\eta_{50} > 0.3$ and $\xi > 1.8$). The adaptive $|z|$-binning maps present the average [S II]/Hα measured in different bins (Section 3.2.2). GAMA CATAIDs and the η_{50} and ξ values are labelled in the plots. The velocity and velocity dispersion contours are equally spaced in 20km s^{-1} intervals. The red dashed circles on the SDSS images indicate approximately the FOV and pointings of the SAMI hexabundles. The dashed lines indicate the galaxy major axes. The inner and outer concentric ellipses correspond to elliptical apertures of $1r_e$ and $1\tilde{r}_e$, respectively. The outer ellipses are approximately 1 arcsec larger than the inner ellipses.

5 HOST GALAXY PROPERTIES

We compute the host galaxy properties before returning to investigate the underlying processes driving the different properties of the extraplanar gas. The host galaxy properties we investigate are stellar mass, star formation rate, star formation history, and their associated quantities. As before, we adopt the photometrically-derived stellar mass from the GAMA survey (Taylor et al. 2011). The following two subsections describe how we measure SFRs using spectral energy distribution (SED) fitting and Hα flux, and star formation histories using the $D_n(4000)$ and Hδ_A indices.

5.1 Star formation rate

To estimate the SFR, we adopt the SED fitting code MAGPHYS described in detail in da Cunha et al. (2008). MAGPHYS is a Bayesian-based package that uses observed photometry to constrain stellar population synthesis models by Bruzual & Charlot (2003) and dust emission of different temperatures from molecular clouds and the diffuse ISM. The UV-to-IR SEDs assume exponential star formation histories of different star formation time-scales with random bursts of star formation superimposed. Physical parameters of the models (SFR, star formation history, stellar mass, dust temperature, etc.) and corresponding errors are constrained by comparing synthesized and observed photometry under a Bayesian

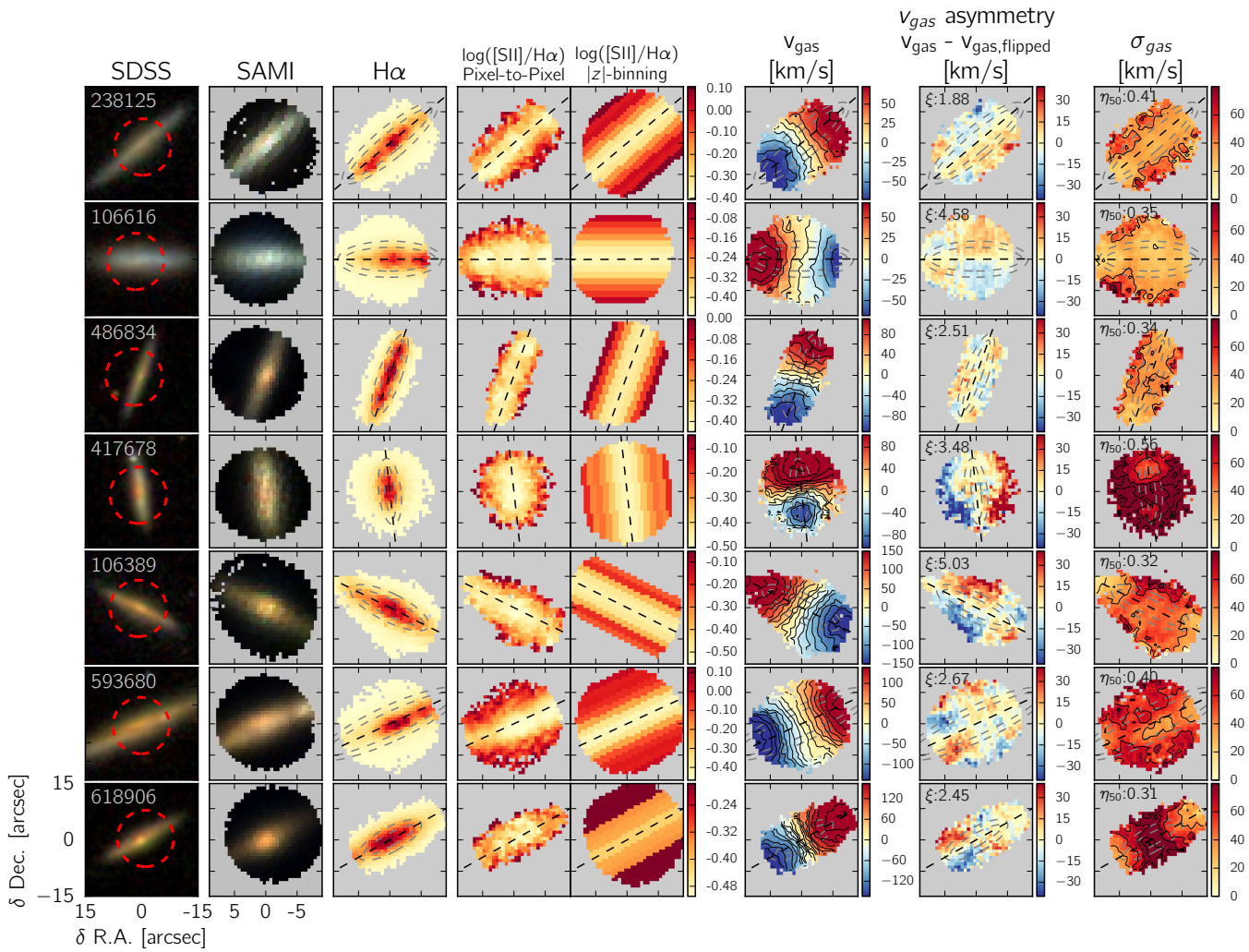

Figure 7 – *continued*

framework. We utilize photometry from the Galaxy Evolution Explorer (GALEX; FUV, NUV; Martin et al. 2005; Wyder et al. 2005), SDSS (*u,g,r,i,z*; Adelman-McCarthy et al. 2008), UKIRT Infrared Deep Sky Survey (UKIDSS) Large Area Survey (Y, J, H, K; Lawrence et al. 2007) and Herschel Space Observatory (Photodetecting Array Camera and Spectrometer: 100μm and 160μm; Spectral and Photometric Imaging Receiver or SPIRE: 250μm, 350μm, and 500μm; Pilbratt et al. 2010; Poglitsch et al. 2010; Griffin et al. 2010). The SDSS and UKIDSS photometry are *r*-band aperture-matched by the GAMA team, and are compiled in their data release 2 (Hill et al. 2011; Liske et al. 2015). The Herschel photometry comes from the Herschel-ATLAS survey (Eales et al. 2010) Phase 1 Internal Data Release. The maps and catalogues will be described in Valiante et al (in preparation) and have been processed in a similar way to that described by Ibar et al. (2010), Pascale et al. (2011) and Rigby et al. (2011). The matching to optical data was performed in a similar way to that described in Smith et al. (2011), and will be presented in Bourne et al. (in preparation). The GALEX, SDSS, and UKIDSS photometry are available for almost all galaxies: 38/40, 40/40, and 39/40, respectively. More than half of our sample (28/40) has photometry from the Herschel-ATLAS survey. Of the 12 galaxies without Herschel photometry, two of them fall outside the Herschel-ATLAS SPIRE footprints and the remainder falls below the detection limits at 250μm.

In addition to the SED-based SFRs, we also calculate SFRs based on the Hα line measured in our integral field data. We construct global, one-dimensional spectra by summing all spaxels in the datacubes, and fit the spectra using the same method described in Section 3.2. The Hα fluxes are extinction corrected using the Balmer decrement method assuming an intrinsic Hα to Hβ line ratio of 2.86 under case-B recombination of T_e of 10,000 K and n_e of 100 cm^{-3} (Osterbrock & Ferland 2006). We adopt the extinction law by Cardelli et al. (1989) of R_V of 3.1. The extinction corrected Hα line fluxes are then converted to SFRs following Murphy et al. (2012). We note that a Chabrier (2003) initial mass function (IMF) is assumed in the Bruzual & Charlot (2003) models used in MAGPHYS, and a Kroupa (2001) IMF is assumed for the Hα SFRs; however the systematic errors due to slight differences between the IMFs are small (within 10%; Bell et al. 2007).

Figure 8 compares the SED- and Hα-based SFRs. The presence of a positive correlation without an appreciable off-

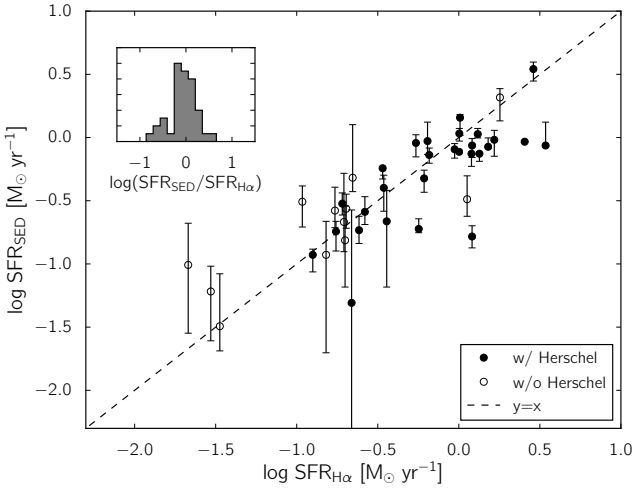

Figure 8. Comparison between SFRs derived from SED fitting using MAGPHYS and from global Hα fluxes measured in our IFS data. Galaxies with Herschel photometry from the Herschel-ATLAS survey are shown as solid circles and the remainders in open circles. The error bars indicate $\pm1\sigma$ confidence intervals reported by MAGPHYS using Bayesian inference. The Hα SFR errors are negligible ($\ll 10\%$) compared to the SFR$_{SED}$ errors and systematic errors due to star formation calibrations. The dashed line is the one-to-one line. The inset shows the distribution of the logarithmic ratios characterised by median $\pm$ standard deviation of -0.02 ± 0.30 dex.

set (approximately -0.02 dex) is encouraging since both SFR diagnostics are subject to different systematic uncertainties and the two SFRs probe star formation of different time-scales (Hα: a few Myr; MAGPHYS: average over the past 100 Myr). The Hα-based SFRs are subject to uncertainties in extinction correction, which can be particularly important in edge-on discs when viewing through prominent dust lanes. Furthermore, correcting for Balmer absorption relies on accurate stellar population synthesis, which can be problematic when the Balmer line equivalent widths are large (i.e. weak emission, strong absorption). Also, the Hα emission could also come from non-thermal ionization by shocks. Finally, although the covering fractions are high (typically $\gtrsim 50\%$), there could still be missing Hα fluxes outside the apertures. The SED-based method depends critically on availability of multi-band photometry (particularly in far infrared), and accurate stellar population synthesis models (see the reviews by Walcher et al. 2011; Conroy 2013). With these caveats, we consider the scatter in Figure 8 as an empirical estimate of the degree of uncertainty in the SFRs (approximately 0.3 dex). We will make use of both types of SFRs and draw qualitative conclusions in a statistical sense.

5.2 Star formation history: D$_n$(4000) and Hδ_A

To quantify the star formation histories, we make use of the classical D$_n$(4000) and Hδ_A indices. Combination of the two indices has been employed as a simple and robust diagnostic to distinguish between continuous and bursty star formation histories (Kauffmann et al. 2003). The D$_n$(4000) index measures the strength of the 4000Å break that monotonically increases with the age of the stellar populations. The Hδ absorption line index, Hδ_A, is sensitive to bursts of star formation, and increases monotonically until peaking at ~ 0.1–1 Gyr after a burst of star formation.

We measure the global D$_n$(4000) and Hδ_A indices on one-dimensional global spectra extracted from the datacubes using elliptical apertures of $1r_e$. The D$_n$(4000) index follows the original definition by Bruzual (1983) but with the narrower passbands proposed by Balogh et al. (1999). Where possible (in 31 out of 40 galaxies), we calibrate our D$_n$(4000) to SDSS DR7 values by comparing D$_n$(4000) measured with data extracted from the same SDSS apertures with those from the MPA-JHU value-added catalog[8]. This empirical correction is to compensate for potential calibration errors in the blue end of the SAMI spectrograph. The multiplication correction factors are typically close to unity ($0.9 - 1.1$). The Hδ_A index measures the absorption equivalent width of Hδ (where positive/negative corresponds absorption/emission) using the passbands defined in the Lick system (Worthey & Ottaviani 1997). To remove contamination from the nebular emission, we include the Hδ emission line in our LZIFU fit and subtract the flux when the line S/N is greater than 3. One galaxy (CATAID:184237) is excluded from the forthcoming comparisons related to star formation history because its weak weak blue continuum does not yield robust index measurements.

6 RESULTS

6.1 Correlation with global quantities

6.1.1 *SFR, SFR surface density, specific SFR, stellar mass and size*

In Figure 9, we present the logarithmic distributions of SFR, SFR surface density ($\Sigma \equiv \mathrm{SFR}/2\pi r_e^2$), specific SFR (sSFR $\equiv$ SFR/M$_*$), stellar mass, and effective radius. We show both SFRs derived from fitting the SED (panels (a), (b) and (c)) and Hα (panels (e), (f) and (g)). The stellar mass and size distributions are shown in panels (d) and (h), respectively. We colour the identified wind-dominated galaxies in red and the remaining galaxies in blue. To test if the two groups of galaxies have similar properties, we perform two-sample Kolmogorov-Smirnov (K-S) tests and Anderson-Darling (A-D) tests, and label the p-values in each panel. A smaller p-value indicates that the two distributions are more likely drawn from different parent populations. Typically, a p-value < 0.05 is considered statistically significant and p-value < 0.01 highly significant (e.g. Taylor 1997). The A-D test is more robust than the K-S test when the differences between cumulative distribution curves are most prominent near the beginning or end of the distributions.

Figure 9 shows that the identified wind-dominated galaxies span wide ranges in SFR, SFR surface density, sSFR, and stellar mass. The wind-dominated galaxies have SFRs as low as approximately 0.1 M$_\odot$ yr^{-1}, and SFR surface densities of approximately 10^{-3} to $10^{-1.5}$ M$_\odot$ yr^{-1} kpc^{-2}, much lower than the canonical threshold found in classical wind galaxies ($\Sigma > 0.1$ M$_\odot$ yr^{-1} kpc^{-2}; Heckman 2002).

[8] http://mpa-garching.mpg.de/SDSS/DR7/

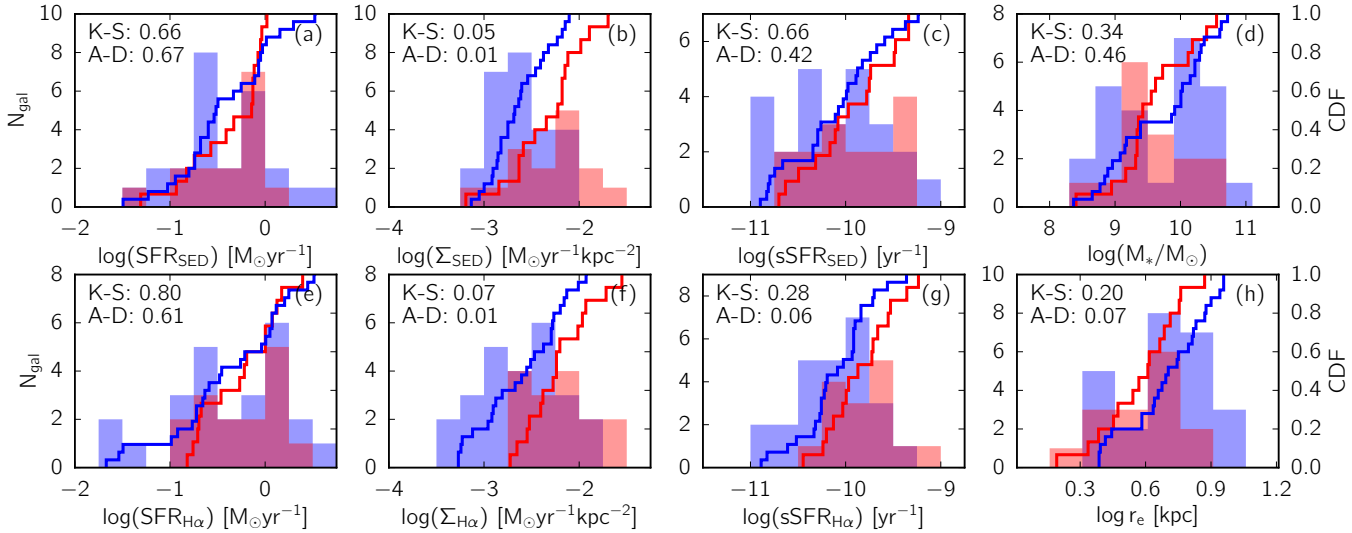

Figure 9. Distributions of the wind-dominated galaxies (red) and the remaining galaxies (blue) in SFR, SFR surface density (Σ), specific SFR (sSFR), stellar mass (M_*) and effective radius (r_e). Both histograms (left axes) and cumulative distributions (CDFs; right axes) are shown. Panels (a), (b) and (c) correspond to SFRs derived from SED fitting, and panels (e), (f) and (g) correspond to those from Hα. The p-values of two-sample Kolmogorov-Smirnov test and Anderson-Darling test are labelled in each panel.

Comparing the distributions of the two groups of galaxies, SFR surface density is the only parameter that presents significantly different distributions for the two groups of galaxies. The wind-dominated galaxies on average have higher SFR surface densities. The same conclusion can be drawn from both the SED- and Hα-based SFRs. The p-values are 0.01 for the A-D tests, and 0.05 and 0.07 for the K-S tests. There is no evidence that the SFR distributions are drawn from different parent populations, indicating that global SFRs do not determine wind activities, but rather that the critical parameter is the spatial concentration of star formation (Section 7.1). The differences in SFR surface density may be partially driven by the differences in size (panel h); the A-D p-value of 0.07 is only marginally higher than the threshold for significance. The only other p-value implying a possible significant difference is from the A-D test of the Hα sSFRs (p-value of 0.06). This may be suggestive of a stronger correlation between winds and more recent star forming activities (a few Myr, as traced by Hα) than the star forming activities on longer time-scales (100 Myr, as traced by MAGPHYS).

6.1.2 Galaxy main sequence

We now combine stellar masses and SFRs to investigate galactic winds on the galaxy main sequence, a log-linear relationship between stellar mass and SFR (Noeske et al. 2007). Figure 10 shows the two groups of galaxies on the galaxy main sequence plane. The dashed lines indicate the galaxy main sequence defined by our sample. We perform an unweighted linear fit to our data (using $\mathrm{SFR_{H\alpha}}$) while fixing the galaxy main sequence slope to well-defined slope of 0.7 (Zahid et al. 2012; Noeske et al. 2007). For comparison, we also show edge-on star-forming discs selected from the SDSS MPA/JHU catalogues (inclination angle $>$ 80 degrees [$b/a < 0.26$] and $0.04 < z < 0.1$). We note that our main sequence is offset below that seen in the literature (e.g. Elbaz et al. 2007; Zahid et al. 2012) because the galaxy main sequence zero point depends on the observed axis ratio. The dashed-lines in Figure 10 are only for visualization purposes, and our conclusions are not affected by the zero point of the galaxy main sequence.

Comparing with the SDSS galaxies, Figure 10 demonstrates that our edge-on discs are indeed part of the normal star forming population in the local Universe. Although these main sequence galaxies have relatively modest SFRs, many of them are still capable of launching large-scale galactic winds that exhibit kinematic signatures resembling the bipolar winds observed in classical wind galaxies (Figure 7). Figure 10 also suggests that the location of a galaxy on the galaxy main sequence plays little, if any, role in governing whether the galaxy hosts galactic winds. The insets of Figure 10 show the distributions of $\Delta \log \mathrm{SFR}$, the difference between measured SFR and that inferred from the galaxy main sequence (dashed lines). The large p-values ($\gg 0.2$) also suggest that the two sets of $\Delta \log \mathrm{SFR_{SED}}$ and $\Delta \log \mathrm{SFR_{H\alpha}}$ distributions are statistically similar. The only exception is the A-D p-value of 0.06 for the Hα SFRs, which is only marginally higher than the threshold for significance. Interestingly, this may again indicate that galactic winds are more sensitive to star forming activities on short time-scales, consistent with the implication from sSFR in Figure 9.

The lack of strong, if any, correlation with the galaxy main sequence is puzzling. The fact that normal galaxies follow the mass-size relation implies that galaxies lying above the galaxy main sequence for a given mass have higher SFRs and higher SFR surface densities than those below the galaxy main sequence (Wuyts et al. 2011). While Figure 9 shows that SFR surface density correlates with the presence of winds, one would expect those high SFR surface density galaxies to occupy the upper part of the galaxy main sequence and therefore a correlation between the presence of winds and the location on the galaxy main sequence. The possibility of exhibiting such a correlation is suggested at a

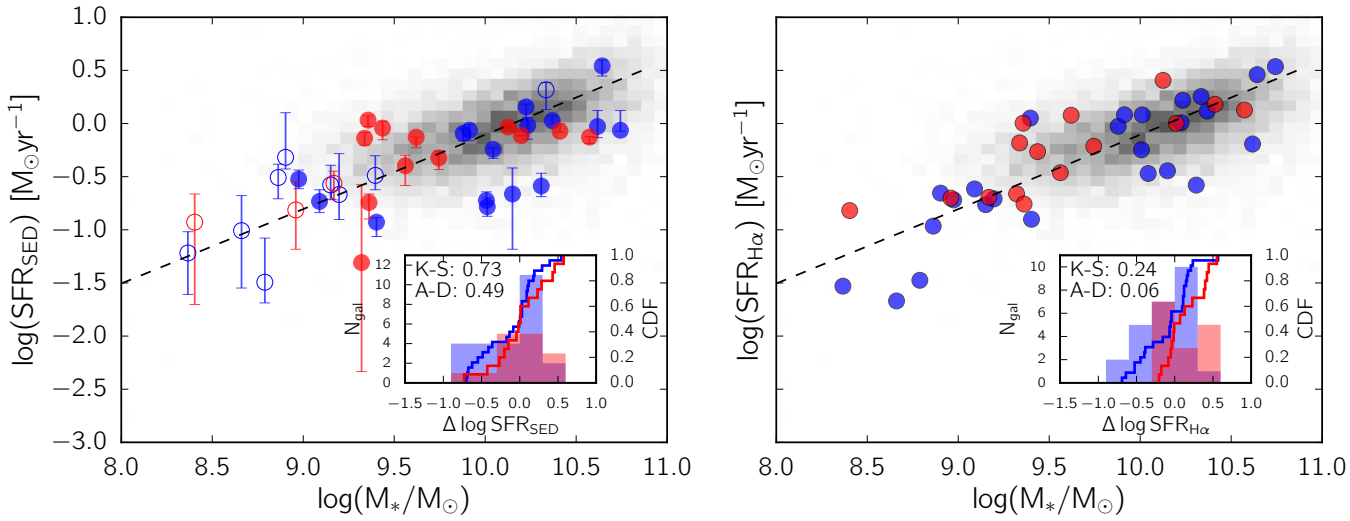

Figure 10. The wind-dominated galaxies (red) and the remaining galaxies (blue) in the star formation versus stellar mass plane. The left and right panels present the SFRs derived from SED fitting and Hα, respectively. The filled and open circles in the left panel correspond to galaxies with and without Herschel photometry. The dashed lines indicate the galaxy main sequence defined by our Hα SFRs. For comparison, the grey scales show distributions of star-forming edge-on discs (inclination angle $>$ 80 degrees or $b/a < 0.26$) in SDSS DR7 from the MPA/JHU catalogue. The insets show the distributions of $\Delta\log$(SFR), the difference between the measured SFR and that inferred from the dashed lines. The p-values of two-sample Kolmogorov-Smirnov test and Anderson-Darling test are labelled in the insets.

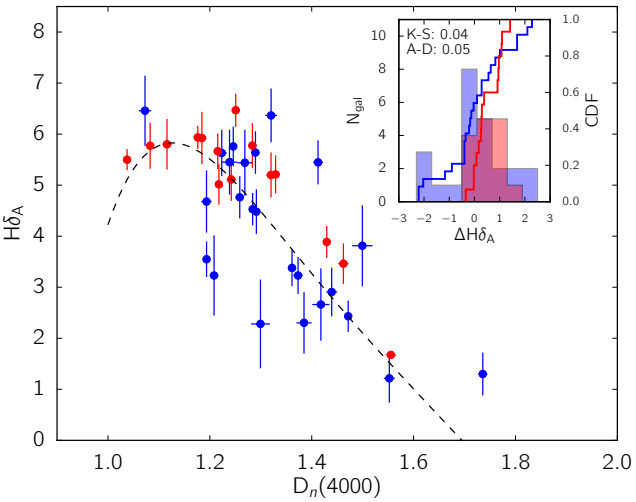

Figure 11. Star formation history traced by D$_n$(4000) and Hδ_A of our galaxies. The wind-dominated galaxies are shown in red, and the remainder of the sample in blue. The dashed curve indicates the median SDSS relation. We fit a fifth order polynomial to the binned SDSS data in Figure 15. The inset shows the distributions of ΔHδ_A, the difference between observed Hδ_A and that inferred from D$_n$(4000) given the median SDSS relation. The histograms correspond to the right y-axis, and the CDFs the left y-axis. The p-values of two-sample Kolmogorov-Smirnov test and Anderson-Darling test are labelled in the inset.

marginal level by the Hα results. However, our data cannot place a firm conclusion due to systematic errors in SFRs, scatter in the mass-size relation and our small sample size.

6.1.3 Star formation history

Figure 11 compares the star formation history traced by D$_n$(4000) and Hδ_A of the two groups of galaxies. The wind-dominated galaxies on average lie above the median D$_n$(4000)-Hδ_A locus of SDSS (12 above and 3 below), whereas the remainder of the sample is distributed evenly above and below the SDSS median (12 above and 12 below). We further demonstrate this observation by showing in the inset of Figure 11 the histograms and cumulative distributions of ΔHδ_A, the difference between observed Hδ_A and that inferred from D$_n$(4000) given the median SDSS relation. The mean ΔHδ_A for the wind-dominated galaxies and the remaining galaxies are 0.51Å and 0.06Å, respectively. The mean ΔHδ_A values can be compared with 0.23 ± 0.21Å and 0.23 ± 0.13Å (mean $\pm$ standard deviation), respectively, if the two populations were distributed randomly, implying that the difference in the mean ΔHδ_A is at about 2σ significance. These mean and standard deviation values characterize the ΔHδ_A distributions resulting from randomly drawing the same numbers of galaxies (as the two groups) 10,000 times from our sample (i.e. Monte Carlo simulations).

The Monte Carlo simulations also suggest that it is very unlikely to observe the configuration of the 15 wind-dominated galaxies, i.e. 12 above and 3 below the SDSS locus. The probability of having more than or equal to 12 galaxies above the SDSS locus is low (6%) when randomly selecting 15 galaxies from our sample. Furthermore, the K-S and A-D tests both yield low probabilities (p-values of 0.04 and 0.05) for the two ΔHδ_A distributions to be drawn from the same parent distribution. We therefore conclude that the wind-dominated galaxies on average show enhanced Hδ_A indices, which presumably are driven by bursts of star formation occurring in the recent past. This conclusion is consistent with the implications in Sections 6.1.1. and 6.1.2

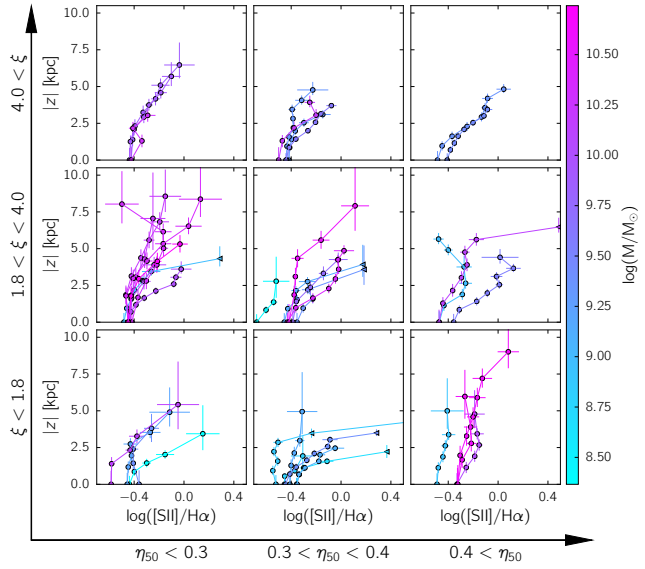

Figure 12. [S II]/Hα line ratio versus off-plane distance $|z|$. The 40 galaxies are presented in 9 different panels depending on their η_{50} and ξ values. The ranges of η_{50} and ξ each panel cover are labelled on the outer large axes (see also Figure 6). Each galaxy corresponds to one set of lines and the colour corresponds to the stellar mass as indicated in the colour bar. The line fluxes are measured with the adaptive $|z|$-binning approach described in Section 3.2. We apply a S/N cut of 3 on both lines and when the [S II] line is not detected we calculate 3σ upper limits assuming 100km s^{-1} line width. Triangles represent upper limits. The horizontal error bars are errors of the line ratio, and the vertical error bars indicate the $|z|$ range covered by each bin.

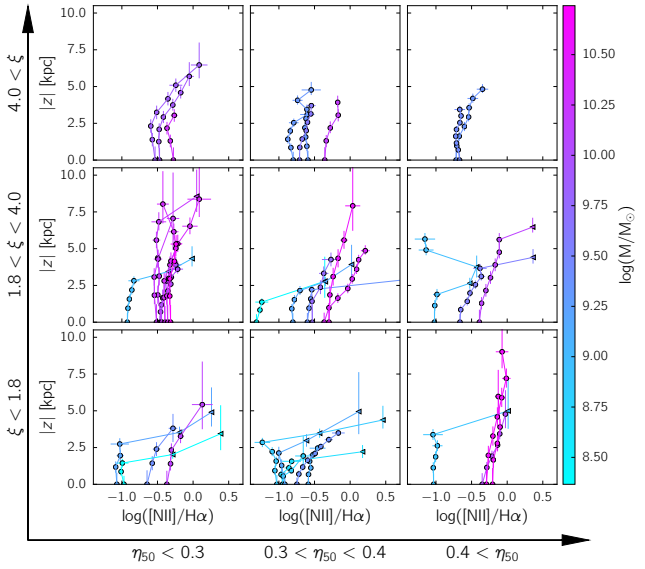

Figure 13. Same as Figure 12 but for the [N II] line.

that the wind activities are more sensitive to star formation of shorter time-scales (i.e. Hα- versus SED-based SFRs in panels (c) and (g) in Figure 10, and Figure 11). We will uss the implications of these results in Section 7.1.

6.2 Optical line ratios

We now examine whether the kinematic properties of the extraplanar gas correlate with the extraplanar emission line ratios. In Figures 2 to 5, we have shown that for galaxies with very different kinematics in their extraplanar gas the emission line ratios can have similar values and show similar increase with increasing $|z|$. Indeed, increase in the emission line ratios with increasing $|z|$ is common for both eDIG and galactic winds. Elevated [N II]/Hα, [S II]/Hα and [O I]/Hα off the disc plane have been observed in the Milky Way and external galaxies that are not currently hosting large-scale galactic winds (e.g. Otte et al. 2002; Miller & Veilleux 2003b; Madsen et al. 2006; Haffner et al. 2009). The enhanced line ratios are considered to be primarily caused by leaking photons from H II regions photoionizing the low density, high temperature extraplanar gas, although additional heating sources such as turbulance, shocks, or cosmic rays could also be important (Collins & Rand 2001; Miller & Veilleux 2003b; Barnes et al. 2014). In classical wind systems (e.g. Sharp & Bland-Hawthorn 2010), these line ratios are also enhanced off the disc plane due to strong forbidden lines of low ionization species emitted by gas in the warm, partially ionized zone in the post-shock regions (Dopita & Sutherland 1995, 1996; Allen et al. 2008). It is of interest to explore in our sample whether the increase in line ratios is different between galaxies with and without strong kinematic perturbations.

We split our galaxies into 9 cells based on η_{50} and ξ and present in Figure 12 their [S II]/Hα line ratio as a function of $|z|$. The line ratios are from the adaptive $|z|$-binning method. Here, we apply a S/N cut of 3 on both the [S II] and Hα lines, and when [S II] is below 3σ we estimate upper limits assuming a 100km s^{-1} line width. The line ratio [S II]/Hα has the advantage of having higher S/N than the weak [O I] line and being less sensitive to the disc abundance and abundance gradient than the [N II]/Hα ratio. Figure 12 shows that in virtually all galaxies the line ratio increases monotonically with $|z|$, and the increase shows no clear correlation with the kinematic properties of the extraplanar gas (i.e. η_{50} and ξ). In other words, the wind-dominated galaxies show the same [S II]/Hα profiles in $|z|$ as those not dominated by galactic winds. Similar comparisons for the [N II]/Hα and [O I]/Hα line ratios are presented in Figures 13 and 14. These $|z|$ profiles also reveal no clear correlations between the line ratio profiles and the kinematic properties of the extraplanar gas. These results indicate that it can be misleading to use only the increase in strong optical line ratios with $|z|$ to infer the presence of either galactic winds or shocks. Even in galaxies with winds or shocks, eDIG could exist and may contaminate or dominate a correlation of line ratio with distance from the disc. Kinematic information such as either velocity asymmetry and/or elevated velocity dispersion must also be considered.

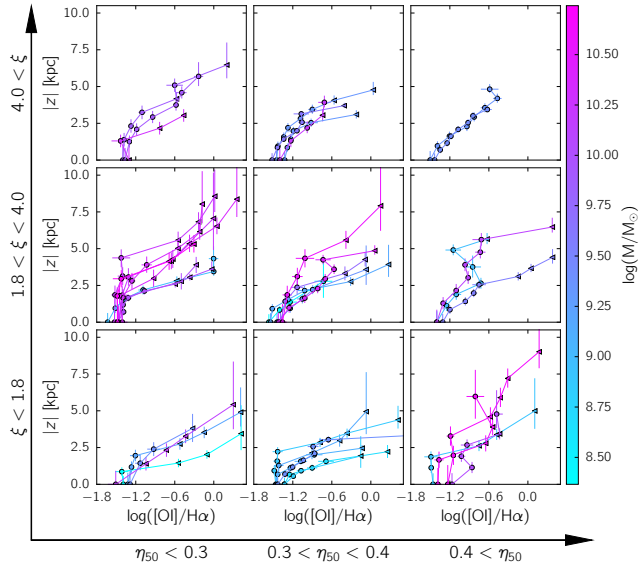

Figure 14. Same as Figure 12 but for the [O I] line.

7 USSION

7.1 The roles of SFR surface density and star formation history in driving galactic winds

The critical role that SFR surface density plays in driving galactic winds has long been recognized. The fact that galactic winds are detected ubiquitously in galaxies with $\Sigma > 0.1 M_{\odot}$ yr^{-1} kpc^{-2} in early studies (see Heckman 2002 for a review) has led to the common notion that there exists a "threshold" in SFR surface density above which winds are driven. The physics behind such a threshold is that this surface density could provide the energy input necessary to exceed the binding energy for the gas to escape into the halo (Chevalier & Clegg 1985; Dopita 2008). The input energy could be thermal energy from supernova or radiation pressure from massive stars (Murray et al. 2005, 2011). The empirical threshold value is met by local starbursts, merging galaxies and high redshift galaxies, but not present-day spirals. The presence of galactic winds in more "normal" galaxies is now revealed by our integral field data and other recent studies (e.g. Chen et al. 2010; Rubin et al. 2014; Ho et al. 2014).

SFR surface density correlates with observed properties of starburst-driven winds, as revealed by several absorption studies using resonant lines (e.g. Na D, Mg II, Fe II; Rubin et al. 2011). Chen et al. (2010) performed a stacking analysis on Na D using SDSS spectra of present-day star-forming galaxies. They found that the equivalent width of the blueshifted (outflowing) component correlates strongly with SFR surface density. At higher redshifts, Bordoloi et al. (2014) coadded the Mg II lines in $z \sim 1$–1.5 galaxies and also found a strong correlation between the equivalent width and SFR surface density. Rubin et al. (2010, 2014) found that such a correlation may still be present, although much less pronounced than others have indicated, in their studies of individual $z \sim 0.5$–1.5 star-forming galaxies using Mg II and Fe II lines. The outflow velocity derived from the absorption line profiles also correlates with SFR surface density (Kornei et al. 2012; Bordoloi et al. 2014), especially when normalized by the galaxy circular velocity (Heckman et al. 2015). Our result of wind-dominated galaxies showing higher SFR surface density further emphasizes the importance of SFR surface density in driving galactic winds (Figure 9).

While the importance of SFR surface density is well-established, SFR surface density is difficult to measure accurately, differs from definition to definition, and could depend on resolution. This makes the comparison of the various figures given in the literature rather nontrivial. The surface area over which star formation rate is divided exhibits a factor of two difference depending on whether one accounts for one side or both sides of the galaxy disc. In general, a characteristic scale radius is required to quantify the area over which the star formation activities spread. It is common to use the effective radius (adopted in this work), isophotal radius, or Petrosian radius. The characteristic scale radius should ideally be measured on a well-resolved rest-frame UV image to better quantify the size of the relevant star-forming disc. However, UV data can be subject to heavy extinction or could be simply unavailable; therefore, images taken at longer wavelengths are sometimes employed instead. In the latter case (including this work), the computed SFR surface density is a lower limit because the actively star-forming disc is typically smaller than the stellar disc that dominates at longer wavelengths. Furthermore, the clumpy-disc morphology at high redshifts raises a concern of over-estimating the star-forming area even when diffraction-limited UV images are available, because much of the area within the scale radius may have no star formation activity. This has motivated some authors to adopt a more sophisticated approach of defining a "clump area" that consists of only pixels above a certain SFR surface density threshold, i.e. counting only the star-forming area (Kornei et al. 2012). While this idea is appealing, the defined area will certainly change with the threshold value and instrumental resolution. Evidently, the SFR surface density first proposed as a global, average quantity is scale-dependent, and depends critically on the area over which the measured star formation rate is averaged.

A second factor that could also control the presence of galactic winds is the star formation history. Our results suggest that large-scale winds trace previous bursts of star formation in the recent past (Section 6.1.3; Figure 11). The potential connection between bursty star formation and galactic winds has already been suggested in a number of studies. Sato et al. (2009) studied the Na D lines at intermediate redshifts ($0.1 < z < 0.6$) with the DEEP2 survey and detected outflows in red-sequence galaxies. They found that many of these galaxies could have experienced recent starbursts as indicated by their enhanced Hβ absorption lines (i.e. poststarburst signatures). Sharp & Bland-Hawthorn (2010) studied 10 local wind galaxies with integral field spectroscopy and found that shock excitation dominates the extended wind-driven, line-emitting filaments in starburst galaxies. A simple time-scale argument demonstrates the need for bursty star formation to excite the filaments. Sharp & Bland-Hawthorn (2010) compared the time evolution of ionizing and mechanical luminosities between an instantaneous burst model and a continuous star formation model. For shock excitation to dominate, the mechanical luminosity has to exceed the ionizing luminosity when the wind-

driven filaments emerge from the disc. For continuous star formation, the ionizing luminosity dominates at all times, whereas for an instantaneous burst, the mechanical luminosity exceeds the ionizing luminosity at about 10 Myr after the burst. This time-scale is comparable to the dynamical time for the filaments to develop (several Myr). Sharp & Bland-Hawthorn (2010) concluded that there is a substantial delay (approximately 10 Myr) after the starburst before the conditions for a large-scale wind are properly established.

The role of bursty star formation is also recognized in numerical simulations. Muratov et al. (2015) analysed hydrodynamic cosmological zoom simulations from the Feedback in Realistic Environments (FIRE; Hopkins et al. 2014) simulations and found that bursts of star formation are followed by powerful blasts of galactic outflows that could sweep gas out to the virial radius. They find that frequent bursts are the dominant form of star formation in all their simulated galaxies, particularly at high redshift. Present-day L^* galaxies that have developed stable discs switch to a continuous mode of star formation and no longer drive large-scale outflows into the haloes, but the bursty form of star formation still persists in sub-L^* galaxies.

If the presence of galactic winds is related to both bursty star formation history and SFR surface density, then one expects a correlation between the two. This is indeed supported by existing SDSS data. Figure 15 shows the median loci of SDSS star-forming galaxies on the $D_n(4000)$ versus $H\delta_A$ plane binned by their SFR surface densities and $D_n(4000)$. Figure 15 clearly demonstrates that galaxies of different SFR surface densities have different star formation histories. Galaxies of higher SFR surface densities on average present higher $H\delta_A$ values at a given $D_n(4000)$ than those with lower SFR surface densities. Excluding the first bin (red) with the highest SFR surface densities, the rest of the bins systematically decrease in $H\delta_A$, especially for $1.1 \lesssim D_n(4000) \lesssim 1.3$. The small differences in $H\delta_A$ are not surprising because 1) the delay time-scale of about 10 Myr corresponds to $H\delta_A$ of approximately 5 to 7Å, substantially smaller than the peak value of approximately 12 to 14Å at a few hundred Myr to one Gyr, and 2) the starburst regions contribute only a fraction of the integrated light as measured by SDSS fibre. We will examine the latter with spatially resolved data in a future work. Despite the small differences in $H\delta_A$, the very small errors of the median (derived from bootstrapping) and the systematic trend all suggest that the SDSS data are entirely consistent with the picture that galaxies of high SFR surface densities have experienced bursts of star formation in the recent past. We expect these galaxies to host large-scale galactic winds. Which of the two physical characteristics is more important in governing the presence of large-scale winds remains to be tested in future works.

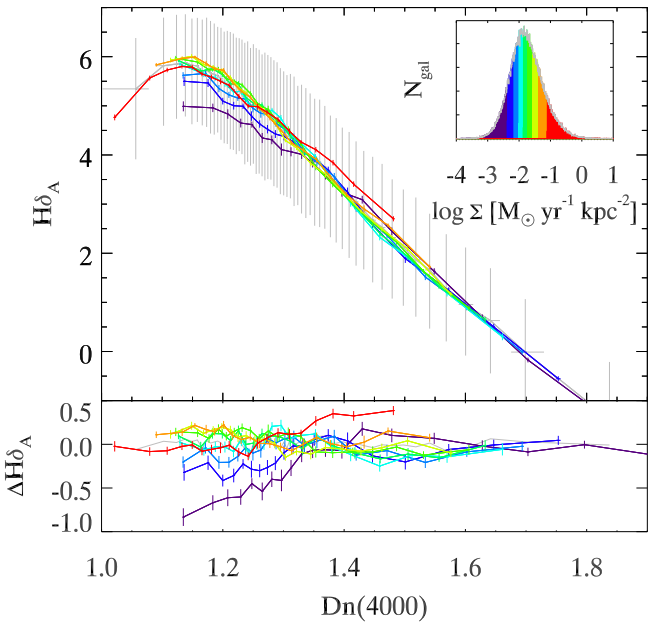

Figure 15. *Upper panel:* $D_n(4000)$ versus $H\delta_A$ for SDSS DR7 star-forming galaxies ($0.04 < z < 0.1$ with non-AGN like [N II]/Hα and [O III]/Hβ line ratios; Kewley et al. 2001). The grey lines connect median values of all the star-forming galaxies ($N_{gal} \approx 112,000$) binned by $D_n(4000)$. The (long) grey error bars contain 68% of the data points in each bin. The colour lines connect median values of sub samples of galaxies binned by Σ and $D_n(4000)$. The corresponding (short) error bars are the bootstrapped 1σ errors of the median. Each colour bin contains approximately 620 galaxies. The inset indicates the distribution of Σ and the different colours correspond to the different Σ bins. *Lower panel:* Differences in $H\delta_A$ between the whole sample and the Σ bins ($\Delta H\delta_A$). A fifth order polynomial is fit to the whole sample (upper panel grey lines) to characterise the overall $H\delta_A(D_n(4000))$. All the values are taken from the MPA/JHU DR7 value-added catalogs (i.e. $D_n(4000)$= `D4000_N_SUB`; $H\delta_A$= `LICK_HD_A_SUB`). We adopt the same definition for SFR surface density as before, i.e. $\Sigma = SFR/2\pi r_e^2$ where r_e is the r-band effective radius.

7.2 Starburst- or AGN-driven winds?

Determining whether the winds are driven by starburst or AGN activities is difficult, but we expect few AGNs in our sample. Only a small fraction ($\lesssim$ 10%) of the emission line galaxies in SDSS contain optical AGNs (Kewley et al. 2001; Trouille & Barger 2010). We also select our sample against optical AGNs using the nuclear optical line ratios (i.e. [N II]/Hα and [O III]/Hβ; Kewley et al. 2001). Although the optical diagnostic could misidentify up to 50% of X-ray AGNs as star-forming galaxies when classified using global spectra (Trouille & Barger 2010; Pons & Watson 2014), the small fraction of AGNs in emission line galaxies means that our sample is unlikely to contain more than four X-ray AGNs. Furthermore, we measure nuclear line ratios from the IFS data, and thus our classification is not subject to optical dilution caused by global emission line fluxes being contaminated by star formation activities in the host galaxies (Moran et al. 2002; Trump et al. 2009). Therefore, we believe that our winds are predominately starburst-driven. This hypothesis is consistent with the strong dependency between wind activities and SFR surface density which matches the theoretical predictions. However, it is impossible to completely rule out previous AGN activities driving the winds due to the rapid flickering of AGNs and the long fading time-scales of the filaments photoionized by the putative AGNs (Novak et al. 2011; Bland-Hawthorn et al. 2013).

7.3 Accretion traced by the extraplanar gas

While in this paper we predominately focus on connecting the extraplanar emissions to galactic winds and eDIG, the extraplanar gas could also be tracing gas accreted onto galaxies through satellite accretion. The best example is the Magellanic Stream seen in the Milky Way which extends more than 100 degrees away from the Magellanic Clouds and travels at approximately 100 to 200 km s^{-1} relatively to the Milky Way (in projection). Kinematic and morphological studies suggest that the Stream is directly related to tidal or hydrodynamical interactions between the Large and Small Magellanic Clouds and the Milky Way, during what could be the clouds' first passage around the Milky Way (Besla et al. 2007). The tip of the leading arm of the Stream has started to interact with the Milky Way disc as revealed by high-resolution H I observations (McClure-Griffiths et al. 2008). Along the Stream, Hα emissions have also been detected and show fairly low velocity dispersions ($\sigma < 40$ km s^{-1}; Weiner & Williams 1996). The Hα surface brightness ranging from a few tens to a few hundreds of milli-Rayleigh can be comparable to the other extraplanar gas off the Milky Way disc plane. Kinematically, the warm ionized gas is found to be associated with H I gas, sharing the same velocity centroids (Weiner & Williams 1996; Putman et al. 2003; Madsen 2012). It has been proposed that the H I-dominated Stream is disrupted while travelling through the hot halo, resulting in shock cascade along the Stream that gives rise to the Hα emission (Bland-Hawthorn et al. 2007; Bland-Hawthorn 2009; Tepper-García et al. 2015).

Satellite accretion events such as the Magellanic Clouds and Stream would naturally yield a high degree of velocity asymmetry (large ξ) but low off-plane velocity dispersion (small η_{50}). In the case of the Milky Way, a high velocity asymmetry value is expected because there are no counterparts to the Magellanic Stream and Clouds north of the galactic plane. Although satellites can in principle accrete on both sides of the discs, it is unlikely that two accretion events (of similar mass and geometry) would occur at the same time on either side of the disc, and therefore we expect in general elevated ξ when a satellite is accreted. The η_{50} parameter, on the other hand, should not increase because the Hα line in the Magellanic Stream shows fairly low velocity dispersions and such low velocity dispersions are expected in the shock cascade model (Tepper-García et al. 2015). Thus, the net effect of satellite accretion on our kinematic diagnostic diagram, Figure 6, is that galaxies with extraplanar gas dominated by satellite accretion would move to the upper left (i.e. high ξ and low η_{50}). The existence of a population of such galaxies is suggested in Figure 6, under the caveat that the η_{50} we measured are subject to the uncertainties of inferring v_{rot} from the Tully-Fisher relation (see Sections 4.2 and 4.3). Follow-up high resolution, wide spatial coverage observations are necessary to study the nature of these kinds of systems.

8 SUMMARY AND CONCLUSIONS

We have examined extraplanar emissions in 40 edge-on disc galaxies using integral field spectroscopy data from the SAMI Galaxy Survey. These galaxies, spanning ranges in $\log(M_*/M_\odot)$ from 8.5 to 11 and $\log(SFR/M_\odot\ yr^{-1})$ from -1.5 to 1, are typical star-forming galaxies that fall on the galaxy main sequence. We have extracted gas velocity maps, velocity dispersion maps and emission line ratio maps from the imaging spectroscopy data to investigate physical properties of the extraplanar gas. Two parameters are invoked to quantify the kinematic properties of the extraplanar gas. The asymmetry parameter describes the asymmetry of the gas motion between the two sides of the disc. The velocity dispersion to rotation ratio parameter quantifies the level of increase in the velocity dispersion of the off-plane gas. These two parameters both increase if the extraplanar gas is predominately perturbed by strong disc-halo interactions through galactic winds, but the two parameters remain small if the disc interacts weakly with the halo, and the extraplanar gas co-rotates with the disc in the form of extended diffuse ionized gas. Using these two empirical parameters, we classify our sample into two groups: those with extraplanar gas dominated by galactic winds ($N_{gal} = 15$) and those not dominated by winds ($N_{gal} = 25$). By comparison of the physical properties of the two groups of galaxies we find that:

- Galactic winds are preferentially detected in galaxies of high SFR surface densities. The wind-dominated galaxies present globally averaged SFR surface densities, i.e. $SFR/2\pi r_e^2$, below the canonical threshold of 0.1 $M_\odot\ yr^{-1}\ kpc^{-2}$.
- Wind-dominated galaxies have enhanced Hδ_A compared to galaxies not dominated by galactic winds, implying that the two groups of galaxies have experienced different star formation histories. Enhanced Hδ_A is consistent with having experienced bursts of star formation in the recent past.
- There are no strong trends with stellar mass, SFR, specific SFR, and locations of galaxies on the galaxy main sequence plane. There are indications of some trends with specific SFR and locations of galaxies on the galaxy main sequence such that galaxies with higher SFRs at a given mass are more likely to drive winds, but we are unable to draw firm conclusions using our data.
- Emission line ratios ([N II]/Hα, [S II]/Hα, and [O I]/Hα) in general increase with increasing off-plane distance, showing no clear correlations with the kinematic properties of the extraplanar gas.

Our results demonstrate that high SFR surface density and bursty star formation history are the two critical physical characteristics governing whether a galaxy is capable of developing large-scale galactic winds. The former is widely recognized in the literature and our results are consistent with a number of studies using other tracers to probe galactic winds. The latter is typically less constrained observationally although a simple time-scale argument concerning the excitation mechanism of the observed wind-driven filaments by Sharp & Bland-Hawthorn (2010) has already implied that classical winds in nearby galaxies are driven by bursts of star formation. Recent hydrodynamic cosmological zoom simulations also suggest that frequent bursts of star formation dominating the star-forming activities are responsible for sweeping gas to the halo. This leads to the prediction that there should exist a correlation between SFR surface density and star formation history. We show that

such correlation is indeed supported by existing SDSS data. SDSS galaxies of high SFR surface densities on average have enhanced $H\delta_A$, consistent with the picture that these galaxies have experienced bursts of star formation in the recent past and are likely to host large-scale winds.

The major implications from this work are that 1) the so-called starburst-driven winds are indeed driven by bursts of star formation, and 2) probing star formation in the time domain is important for finding galactic winds and understanding how such disc-halo interactions affect the cycle of baryonic matter as galaxies evolve over cosmic time.

ACKNOWLEDGMENTS

We thank the anonymous referee for the thorough review and constructive comments. ITH thanks Ken Freeman, Elisabete da Cunha, Laura Zschaechner, Catharine Wu, and George Heald for useful ussions. AMM, MAD and LJK acknowledge the support of the Australian Research Council (ARC) through overy project DP130103925. MAD would also like to thank the Deanship of Scientific Research (DSR), King Abdulaziz University for additional financial support as Distinguished Visiting Professor under the KAU Hi-Ci program. BG gratefully acknowledges the support of the ARC as the recipient of a Future Fellowship (FT140101202). JTA acknowledges the award of a SIEF John Stocker Fellowship. NB acknowledges the support of the EC FP7 SPACE project ASTRODEEP (Ref. No. 312725). JBH is funded by an ARC Laureate Fellowship. LC acknowledges financial support from the ARC (DP130100664). LD acknowledges support from the European Research Council Advanced Investigator grant, COSMICISM.

The SAMI Galaxy Survey is based on observations made at the Anglo-Australian Telescope. The Sydney-AAO Multi-object Integral field spectrograph was developed jointly by the University of Sydney and the Australian Astronomical Observatory. The SAMI input catalogue is based on data taken from the Sloan Digital Sky Survey, the GAMA Survey and the VST ATLAS Survey. The SAMI Galaxy Survey is funded by the Australian Research Council Centre of Excellence for All-sky Astrophysics, through project number CE110001020, and other participating institutions. The SAMI Galaxy Survey website is http://sami-survey.org/.

GAMA is a joint European-Australasian project based around a spectroscopic campaign using the Anglo-Australian Telescope. The GAMA input catalogue is based on data taken from the Sloan Digital Sky Survey and the UKIRT Infrared Deep Sky Survey. Complementary imaging of the GAMA regions is being obtained by a number of independent survey programmes including GALEX MIS, VST KiDS, VISTA VIKING, WISE, Herschel-ATLAS, GMRT and ASKAP providing UV to radio coverage. GAMA is funded by the STFC (UK), the ARC (Australia), the AAO, and the participating institutions. The GAMA website is http://www.gama-survey.org/.

The Herschel-ATLAS is a project with Herschel, which is an ESA space observatory with science instruments provided by European-led Principal Investigator consortia and with important participation from NASA. The H-ATLAS website is http://www.h-atlas.org/.

Funding for the Sloan Digital Sky Survey (SDSS) and SDSS-II has been provided by the Alfred P. Sloan Foundation, the Participating Institutions, the National Science Foundation, the U.S. Department of Energy, the National Aeronautics and Space Administration, the Japanese Monbukagakusho, and the Max Planck Society, and the Higher Education Funding Council for England. The SDSS Web site is http://www.sdss.org/.

REFERENCES

Adelman-McCarthy J. K., et al., 2008, ApJS, 175, 297
Allen M. G., Groves B. A., Dopita M. A., Sutherland R. S., Kewley L. J., 2008, ApJS, 178, 20
Allen J. T., et al., 2015, MNRAS, 446, 1567
Axon D. J., Taylor K., 1978, Nature, 274, 37
Balogh M. L., Morris S. L., Yee H. K. C., Carlberg R. G., Ellingson E., 1999, ApJ, 527, 54
Barnes J. E., Wood K., Hill A. S., Haffner L. M., 2014, MNRAS, 440, 3027
Bell E. F., de Jong R. S., 2001, ApJ, 550, 212
Bell E. F., Zheng X. Z., Papovich C., Borch A., Wolf C., Meisenheimer K., 2007, ApJ, 663, 834
Besla G., Kallivayalil N., Hernquist L., Robertson B., Cox T. J., van der Marel R. P., Alcock C., 2007, ApJ, 668, 949
Bland J., Tully B., 1988, Nature, 334, 43
Bland-Hawthorn J., 2009, in Andersen J., Nordströara m B., Bland-Hawthorn J., eds, IAU Symposium Vol. 254, IAU Symposium. pp 241–254 (arXiv:0811.2467), doi:10.1017/S174392130802766X
Bland-Hawthorn J., Sutherland R., Agertz O., Moore B., 2007, ApJ, 670, L109
Bland-Hawthorn J., Maloney P. R., Sutherland R. S., Madsen G. J., 2013, ApJ, 778, 58
Bordoloi R., et al., 2014, ApJ, 794, 130
Bregman J. N., 1980, ApJ, 236, 577
Bruzual A. G., 1983, ApJ, 273, 105
Bruzual G., Charlot S., 2003, MNRAS, 344, 1000
Bryant J. J., et al., 2015, MNRAS, 447, 2857
Bundy K., et al., 2015, ApJ, 798, 7
Cappellari M., Emsellem E., 2004, PASP, 116, 138
Cardelli J. A., Clayton G. C., Mathis J. S., 1989, ApJ, 345, 245
Cecil G., Bland-Hawthorn J., Veilleux S., Filippenko A. V., 2001, ApJ, 555, 338
Cecil G., Bland-Hawthorn J., Veilleux S., 2002, ApJ, 576, 745
Cecil G., et al., 2015, preprint, (arXiv:1511.05445)
Chabrier G., 2003, PASP, 115, 763
Chen Y.-M., Tremonti C. A., Heckman T. M., Kauffmann G., Weiner B. J., Brinchmann J., Wang J., 2010, AJ, 140, 445
Chevalier R. A., Clegg A. W., 1985, Nature, 317, 44
Collins J. A., Rand R. J., 2001, ApJ, 551, 57
Conroy C., 2013, ARA&A, 51, 393
Croom S., Saunders W., Heald R., 2004, Anglo-Australian Observatory Epping Newsletter, 106, 12
Croom S. M., et al., 2012, MNRAS, 421, 872
Di Teodoro E. M., Fraternali F., 2015, MNRAS, 451, 3021
Dopita M. A., 2008, in Bresolin F., Crowther P. A., Puls J., eds, IAU Symposium Vol. 250, IAU Symposium. pp 367–378, doi:10.1017/S1743921308020711
Dopita M. A., Sutherland R. S., 1995, ApJ, 455, 468
Dopita M. A., Sutherland R. S., 1996, ApJS, 102, 161
Dove J. B., Shull J. M., 1994, ApJ, 430, 222
Driver S. P., et al., 2009, Astronomy and Geophysics, 50, 050000
Eales S., et al., 2010, PASP, 122, 499
Elbaz D., et al., 2007, A&A, 468, 33
Fogarty L. M. R., et al., 2012, ApJ, 761, 169

Fraternali F., Oosterloo T. A., Sancisi R., Swaters R., 2005, in Braun R., ed., Astronomical Society of the Pacific Conference Series Vol. 331, Extra-Planar Gas. p. 239 (arXiv:astro-ph/0410375)
Fruchter A. S., Hook R. N., 2002, PASP, 114, 144
González Delgado R. M., Cerviño M., Martins L. P., Leitherer C., Hauschildt P. H., 2005, MNRAS, 357, 945
Griffin M. J., et al., 2010, A&A, 518, L3
Haffner L. M., et al., 2009, Reviews of Modern Physics, 81, 969
Heald G. H., Rand R. J., Benjamin R. A., Collins J. A., Bland-Hawthorn J., 2006a, ApJ, 636, 181
Heald G. H., Rand R. J., Benjamin R. A., Bershady M. A., 2006b, ApJ, 647, 1018
Heald G. H., Rand R. J., Benjamin R. A., Bershady M. A., 2007, ApJ, 663, 933
Heckman T. M., 2002, in Mulchaey J. S., Stocke J. T., eds, Astronomical Society of the Pacific Conference Series Vol. 254, Extragalactic Gas at Low Redshift. p. 292 (arXiv:astro-ph/0107438)
Heckman T. M., Armus L., Miley G. K., 1990, ApJS, 74, 833
Heckman T. M., Alexandroff R. M., Borthakur S., Overzier R., Leitherer C., 2015, ApJ, 809, 147
Hill D. T., et al., 2011, MNRAS, 412, 765
Ho I.-T., et al., 2014, MNRAS, 444, 3894
Hopkins P. F., Kereš D., Oñorbe J., Faucher-Giguère C.-A., Quataert E., Murray N., Bullock J. S., 2014, MNRAS, 445, 581
Hubble E. P., 1926, ApJ, 64, 321
Ibar E., et al., 2010, MNRAS, 409, 38
Józsa G. I. G., Kenn F., Klein U., Oosterloo T. A., 2007, A&A, 468, 731
Kauffmann G., et al., 2003, MNRAS, 341, 33
Kelvin L. S., et al., 2012, MNRAS, 421, 1007
Kewley L. J., Dopita M. A., Sutherland R. S., Heisler C. A., Trevena J., 2001, ApJ, 556, 121
Kornei K. A., Shapley A. E., Martin C. L., Coil A. L., Lotz J. M., Schiminovich D., Bundy K., Noeske K. G., 2012, ApJ, 758, 135
Kroupa P., 2001, MNRAS, 322, 231
Lawrence A., et al., 2007, MNRAS, 379, 1599
Leroy A. K., et al., 2015, ApJ, 814, 83
Liske J., et al., 2015, MNRAS, 452, 2087
Madsen G. J., 2012, in de Avillez M. A., ed., EAS Publications Series Vol. 56, EAS Publications Series. pp 281–284, doi:10.1051/eas/1256045
Madsen G. J., Reynolds R. J., Haffner L. M., 2006, ApJ, 652, 401
Markwardt C. B., 2009, in Bohlender D. A., Durand D., Dowler P., eds, Astronomical Society of the Pacific Conference Series Vol. 411, Astronomical Data Analysis Software and Systems XVIII. p. 251 (arXiv:0902.2850)
Martin D. C., et al., 2005, ApJ, 619, L1
Martin C. L., Shapley A. E., Coil A. L., Kornei K. A., Bundy K., Weiner B. J., Noeske K. G., Schiminovich D., 2012, ApJ, 760, 127
McClure-Griffiths N. M., et al., 2008, ApJ, 673, L143
Ménard B., Scranton R., Fukugita M., Richards G., 2010, MNRAS, 405, 1025
Miller III W. W., Cox D. P., 1993, ApJ, 417, 579
Miller S. T., Veilleux S., 2003a, ApJS, 148, 383
Miller S. T., Veilleux S., 2003b, ApJ, 592, 79
Moran E. C., Filippenko A. V., Chornock R., 2002, ApJ, 579, L71
Muratov A. L., Kereš D., Faucher-Giguère C.-A., Hopkins P. F., Quataert E., Murray N., 2015, MNRAS, 454, 2691
Murphy E. J., et al., 2012, ApJ, 761, 97
Murray N., Quataert E., Thompson T. A., 2005, ApJ, 618, 569
Murray N., Ménard B., Thompson T. A., 2011, ApJ, 735, 66
Noeske K. G., et al., 2007, ApJ, 660, L43
Norman C. A., Ikeuchi S., 1989, ApJ, 345, 372
Novak G. S., Ostriker J. P., Ciotti L., 2011, ApJ, 737, 26
Osterbrock D. E., Ferland G. J., 2006, Astrophysics of gaseous nebulae and active galactic nuclei
Otte B., Reynolds R. J., Gallagher III J. S., Ferguson A. M. N., 2001, ApJ, 560, 207
Otte B., Gallagher III J. S., Reynolds R. J., 2002, ApJ, 572, 823
Pascale E., et al., 2011, MNRAS, 415, 911
Peek J. E. G., Ménard B., Corrales L., 2015, ApJ, 813, 7
Peng C. Y., Ho L. C., Impey C. D., Rix H.-W., 2010, AJ, 139, 2097
Pilbratt G. L., et al., 2010, A&A, 518, L1
Poglitsch A., et al., 2010, A&A, 518, L2
Pons E., Watson M. G., 2014, A&A, 568, A108
Putman M. E., Bland-Hawthorn J., Veilleux S., Gibson B. K., Freeman K. C., Maloney P. R., 2003, ApJ, 597, 948
Reynolds R. J., Scherb F., Roesler F. L., 1973, ApJ, 185, 869
Reynolds R. J., Haffner L. M., Tufte S. L., 1999, ApJ, 525, L21
Rich J. A., Dopita M. A., Kewley L. J., Rupke D. S. N., 2010, ApJ, 721, 505
Rich J. A., Kewley L. J., Dopita M. A., 2011, ApJ, 734, 87
Rigby E. E., et al., 2011, MNRAS, 415, 2336
Rossa J., Dettmar R.-J., 2000, A&A, 359, 433
Rossa J., Dettmar R.-J., 2003a, A&A, 406, 493
Rossa J., Dettmar R.-J., 2003b, A&A, 406, 505
Rossa J., Dettmar R.-J., Walterbos R. A. M., Norman C. A., 2004, AJ, 128, 674
Rubin K. H. R., Weiner B. J., Koo D. C., Martin C. L., Prochaska J. X., Coil A. L., Newman J. A., 2010, ApJ, 719, 1503
Rubin K. H. R., Prochaska J. X., Ménard B., Murray N., Kasen D., Koo D. C., Phillips A. C., 2011, ApJ, 728, 55
Rubin K. H. R., Prochaska J. X., Koo D. C., Phillips A. C., Martin C. L., Winstrom L. O., 2014, ApJ, 794, 156
Rupke D. S. N., Veilleux S., 2013, ApJ, 775, L15
Saha K., de Jong R., Holwerda B., 2009, MNRAS, 396, 409
Sánchez S. F., et al., 2012, A&A, 538, A8
Sato T., Martin C. L., Noeske K. G., Koo D. C., Lotz J. M., 2009, ApJ, 696, 214
Saunders W., et al., 2004, in Moorwood A. F. M., Iye M., eds, Society of Photo-Optical Instrumentation Engineers (SPIE) Conference Series Vol. 5492, Ground-based Instrumentation for Astronomy. pp 389–400, doi:10.1117/12.550871
Schroetter I., Bouché N., Péroux C., Murphy M. T., Contini T., Finley H., 2015, ApJ, 804, 83
Seon K.-I., 2009, ApJ, 703, 1159
Shapiro P. R., Field G. B., 1976, ApJ, 205, 762
Sharp R. G., Bland-Hawthorn J., 2010, ApJ, 711, 818
Sharp R., et al., 2006, in Society of Photo-Optical Instrumentation Engineers (SPIE) Conference Series. p. 0 (arXiv:astro-ph/0606137), doi:10.1117/12.671022
Sharp R., et al., 2015, MNRAS, 446, 1551
Shopbell P. L., Bland-Hawthorn J., 1998, ApJ, 493, 129
Smith G. A., et al., 2004, in Moorwood A. F. M., Iye M., eds, Society of Photo-Optical Instrumentation Engineers (SPIE) Conference Series Vol. 5492, Ground-based Instrumentation for Astronomy. pp 410–420, doi:10.1117/12.551013
Smith D. J. B., et al., 2011, MNRAS, 416, 857
Sofue Y., Rubin V., 2001, ARA&A, 39, 137
Steidel C. C., Erb D. K., Shapley A. E., Pettini M., Reddy N., Bogosavljević M., Rudie G. C., Rakic O., 2010, ApJ, 717, 289
Taylor J., 1997, Introduction to Error Analysis, the Study of Uncertainties in Physical Measurements, 2nd Edition. University Science Books
Taylor E. N., et al., 2011, MNRAS, 418, 1587
Tepper-García T., Bland-Hawthorn J., Sutherland R. S., 2015, ApJ, 813, 94
Tonry J. L., Blakeslee J. P., Ajhar E. A., Dressler A., 2000, ApJ, 530, 625

Tremonti C. A., Moustakas J., Diamond-Stanic A. M., 2007, ApJ, 663, L77
Trouille L., Barger A. J., 2010, ApJ, 722, 212
Trump J. R., et al., 2009, ApJ, 706, 797
Tumlinson J., et al., 2011, Science, 334, 948
Veilleux S., Rupke D. S., 2002, ApJ, 565, L63
Veilleux S., Cecil G., Bland-Hawthorn J., Tully R. B., Filippenko A. V., Sargent W. L. W., 1994, ApJ, 433, 48
Veilleux S., Cecil G., Bland-Hawthorn J., 2005, ARA&A, 43, 769
Veilleux S., et al., 2013, ApJ, 776, 27
Vogt F. P. A., Dopita M. A., Kewley L. J., 2013, ApJ, 768, 151
Walcher J., Groves B., Budavári T., Dale D., 2011, Ap&SS, 331, 1
Weiner B. J., Williams T. B., 1996, AJ, 111, 1156
Weiner B. J., et al., 2009, ApJ, 692, 187
Werk J. K., Prochaska J. X., Thom C., Tumlinson J., Tripp T. M., O'Meara J. M., Peeples M. S., 2013, ApJS, 204, 17
Werk J. K., et al., 2014, ApJ, 792, 8
Westmoquette M. S., Smith L. J., Gallagher III J. S., 2011, MNRAS, 414, 3719
Wild V., et al., 2014, A&A, 567, A132
Worthey G., Ottaviani D. L., 1997, ApJS, 111, 377
Wuyts S., et al., 2011, ApJ, 742, 96
Wyder T. K., et al., 2005, ApJ, 619, L15
York D. G., et al., 2000, AJ, 120, 1579
Zahid H. J., Dima G. I., Kewley L. J., Erb D. K., Davé R., 2012, ApJ, 757, 54
Zschaechner L. K., Rand R. J., Walterbos R., 2015, ApJ, 799, 61
Zurita A., Rozas M., Beckman J. E., 2000, A&A, 363, 9
Zurita A., Beckman J. E., Rozas M., Ryder S., 2002, A&A, 386, 801
da Cunha E., Charlot S., Elbaz D., 2008, MNRAS, 388, 1595
de Avillez M. A., 2000, Ap&SS, 272, 23

APPENDIX A: ADDITIONAL FIGURES AND TABLE

Figure A1 presents the 25 galaxies not classified as wind-dominated, i.e. $\eta_{50} < 0.3$ or $\xi < 1.8$ (see Section 4.3). The wind-dominated galaxies are presented in Figure 7. We summarise the basic properties of our sample in Table A1.

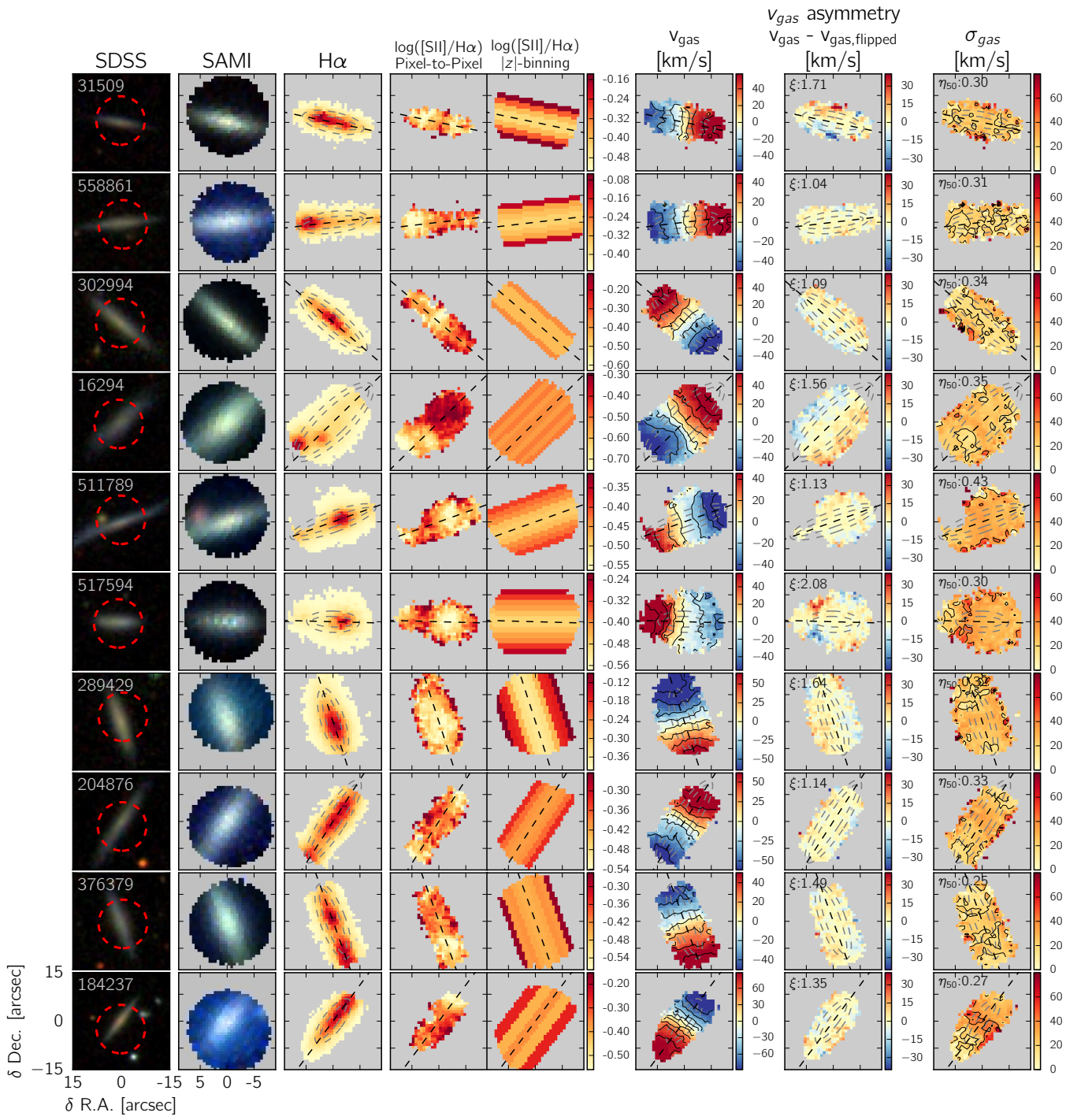

Figure A1. Same as Figure 7 but for galaxies not dominated by galactic winds (i.e. $\eta_{50} < 0.3$ or $\xi < 1.8$).

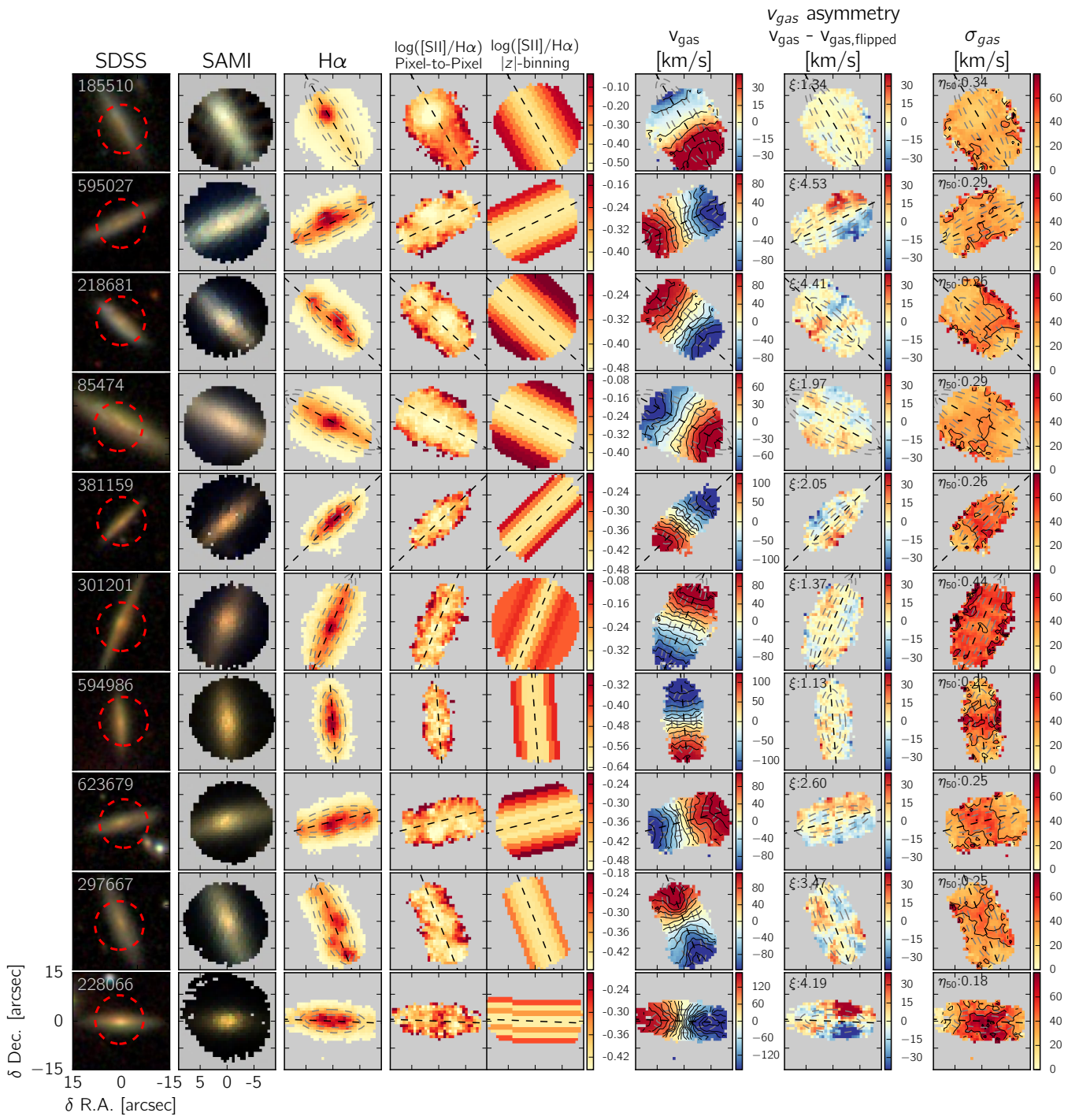

Figure A1 – *continued*

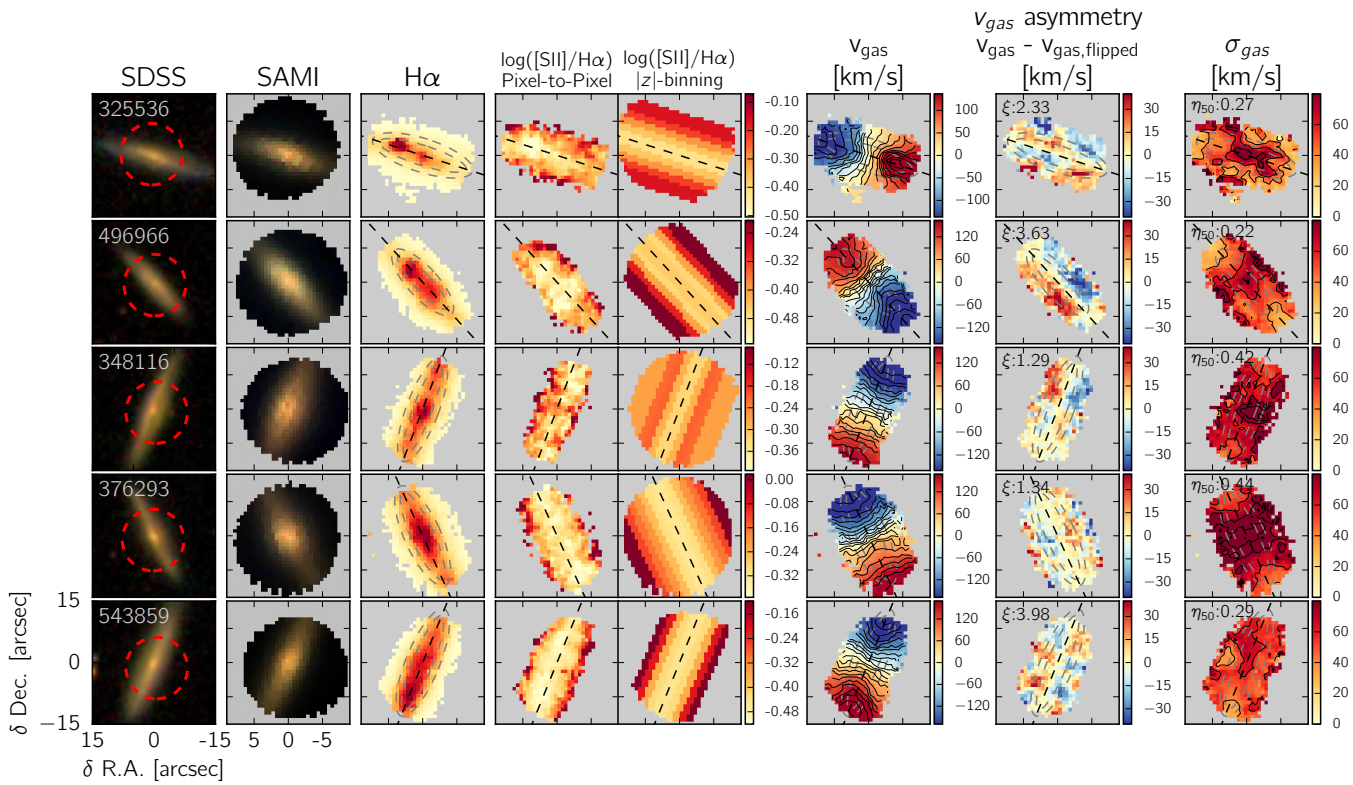

Figure A1 – *continued*

Table A1. Sample properties

GAMA CATAID	R.A. [°]	Dec. [°]	z^a –	D^b [Mpc]	r_e [″]/[kpc]	$\log(M_*)$ [$M_\odot$]	$\mathrm{SFR_{SED}}$ [$M_\odot$ yr^{-1}]	$\mathrm{SFR_{H\alpha}}$	$\log \Sigma_{\mathrm{SED}}$ [$M_\odot$ yr^{-1} kpc^{-2}]	$\log \Sigma_{\mathrm{H\alpha}}$	$\mathrm{D_n(4000)}$ –	$\mathrm{H\delta_A}$ [Å]	ξ –	η_{50}^c –
wind-dominated														
543769	212.8001	−0.9674	0.0249	113.0	2.8/1.6	8.4	$0.12^{+0.10}_{-0.10}$	0.15	−2.111	−2.002	1.12	5.8 ± 0.5	2.57	0.31*
93167	219.2504	+0.5647	0.0348	156.4	5.4/4.1	9.0	$0.15^{+0.13}_{-0.09}$	0.20	−2.836	−2.725	1.18	5.9 ± 0.5	2.36	0.44
24433	185.7224	+1.2413	0.0278	126.9	4.0/2.4	9.2	$0.27^{+0.08}_{-0.08}$	0.20	−2.135	−2.266	1.28	5.8 ± 0.4	2.15	0.31*
567624	212.5595	−0.5785	0.0258	116.6	6.2/3.5	9.3	$0.05^{+0.22}_{-0.04}$	0.22	−3.191	−2.544	1.25	6.5 ± 0.3	4.11	0.32
574200	134.5234	−0.0211	0.0286	129.6	4.7/3.0	9.3	$0.73^{+0.10}_{-0.10}$	0.66	−1.883	−1.928	1.22	5.0 ± 0.4	5.31	0.40*
228432	217.3857	+1.1174	0.0298	134.0	4.4/2.9	9.4	$1.08^{+0.10}_{-0.14}$	1.01	−1.681	−1.710	1.08	5.8 ± 0.5	4.09	0.43*
239249	217.0184	+1.6391	0.0290	130.7	3.5/2.2	9.4	$0.18^{+0.04}_{-0.05}$	0.17	−2.222	−2.236	1.24	5.1 ± 0.4	1.96	0.33*
31452	179.8635	−1.1551	0.0202	95.7	10.0/4.6	9.4	$0.91^{+0.15}_{-0.20}$	0.54	−2.174	−2.396	1.04	5.5 ± 0.2	11.88	0.49
238125	213.3289	+1.6644	0.0259	117.0	8.7/4.9	9.6	$0.40^{+0.10}_{-0.14}$	0.34	−2.580	−2.645	1.22	5.7 ± 0.3	1.88	0.41
106616	216.7211	+0.9629	0.0262	118.0	7.3/4.2	9.6	$0.74^{+0.00}_{-0.15}$	1.20	−2.167	−1.960	1.18	5.9 ± 0.2	4.58	0.35
486834	221.7448	−1.7889	0.0435	195.9	6.0/5.7	9.7	$0.48^{+0.08}_{-0.11}$	0.61	−2.630	−2.521	1.33	5.2 ± 0.4	2.51	0.34
417678	132.7382	+2.3462	0.0394	178.9	4.3/3.7	10.1	$0.93^{+0.01}_{-0.01}$	2.55	−1.979	−1.539	1.32	5.2 ± 0.4	3.48	0.56*
106389	215.9010	+1.0076	0.0401	180.8	5.9/5.2	10.2	$0.77^{+0.00}_{-0.01}$	1.00	−2.344	−2.229	1.46	3.5 ± 0.4	5.03	0.32
593680	217.4419	−0.1524	0.0300	135.1	11.5/7.5	10.4	$0.85^{+0.15}_{-0.02}$	1.52	−2.626	−2.372	1.43	3.9 ± 0.3	2.67	0.40
618906	217.3594	+0.3976	0.0565	256.3	4.7/5.8	10.6	$0.74^{+0.01}_{-0.10}$	1.34	−2.451	−2.196	1.56	1.7 ± 0.4	2.45	0.31*
not wind-dominated														
31509	179.9708	−1.0899	0.0260	119.4	4.8/2.8	8.4	$0.06^{+0.04}_{-0.04}$	0.03	−2.907	−3.219	1.24	5.5 ± 0.6	1.71	0.30*
558861	174.2570	−0.5120	0.0194	92.2	5.6/2.5	8.7	$0.10^{+0.11}_{-0.07}$	0.02	−2.602	−3.264	1.50	3.8 ± 0.8	1.04	0.31
302994	140.1432	+1.5511	0.0167	76.4	7.1/2.6	8.8	$0.03^{+0.05}_{-0.01}$	0.03	−3.134	−3.115	1.26	4.8 ± 0.4	1.09	0.34
16294	218.2074	+0.6370	0.0290	130.4	9.0/5.7	8.9	$0.31^{+0.10}_{-0.11}$	0.11	−2.812	−3.270	1.19	4.7 ± 0.6	1.56	0.35
511789	215.9925	−1.1284	0.0344	154.9	7.4/5.6	8.9	$0.48^{+0.78}_{-0.11}$	0.22	−2.609	−2.946	1.32	6.4 ± 0.5	1.13	0.43
517594	132.9978	+2.5434	0.0285	129.3	3.9/2.4	9.0	$0.30^{+0.06}_{-0.06}$	0.19	−2.095	−2.291	1.07	6.5 ± 0.7	2.08	0.30*
289429	182.3047	+1.8366	0.0194	92.5	5.5/2.5	9.1	$0.18^{+0.05}_{-0.04}$	0.24	−2.314	−2.197	1.21	3.2 ± 0.8	1.64	0.32
204876	139.8844	−0.4101	0.0387	175.7	8.0/6.8	9.2	$0.26^{+0.14}_{-0.07}$	0.17	−3.046	−3.232	1.27	5.4 ± 0.6	1.14	0.33
376379	133.0553	+1.4996	0.0357	161.8	6.4/5.0	9.2	$0.21^{+0.31}_{-0.09}$	0.20	−2.863	−2.904	1.22	5.6 ± 0.5	1.49	0.25
184237	175.7381	−1.5391	0.0434	197.7	4.0/3.8	9.4	$0.33^{+0.17}_{-0.09}$	1.13	−2.453	−1.914	–	–	1.35	0.27*
185510	180.5913	−1.4539	0.0205	96.6	8.2/3.8	9.4	$0.12^{+0.01}_{-0.03}$	0.13	−2.895	−2.868	1.25	5.8 ± 0.4	1.34	0.34
595027	223.1331	−0.1664	0.0425	191.1	7.2/6.6	9.9	$0.81^{+0.09}_{-0.12}$	0.94	−2.534	−2.466	1.29	5.6 ± 0.4	4.53	0.29
218681	139.2505	+0.8441	0.0380	172.5	5.2/4.4	9.9	$0.86^{+0.12}_{-0.17}$	1.21	−2.140	−1.995	1.28	4.5 ± 0.3	4.41	0.26*
85474	182.5694	+0.6266	0.0207	97.4	9.7/4.6	10.0	$0.19^{+0.04}_{-0.01}$	0.57	−2.845	−2.369	1.19	3.5 ± 0.3	1.97	0.29

[a] Redshift

[b] Luminosity distance inferred from redshift after correcting for the local and large-scale flows (Tonry et al. 2000).

[c] Those with asterisk (*) have v_{rot} measured from the data. The others have v_{rot} inferred from the Tully-Fisher relation (see Section 4.2).

Table A1 – *continued* Sample properties

GAMA CATAID	R.A. [°]	Dec. [°]	z^a –	D^b [Mpc]	r_e [″]/[kpc]	$\log(M_*)$ [$M_\odot$]	$\mathrm{SFR_{SED}}$ [$M_\odot$ yr^{-1}]	$\mathrm{SFR_{H\alpha}}$	$\log \Sigma_{\mathrm{SED}}$ [$M_\odot$ yr^{-1}	$\log \Sigma_{\mathrm{H\alpha}}$ kpc^{-2}]	$\mathrm{D_n(4000)}$ –	$\mathrm{H\delta_A}$ [Å]	ξ –	η^c_{50} –
381159	131.6598	+1.7285	0.0505	229.4	4.6/5.1	10.0	$0.16^{+0.04}_{-0.03}$	1.21	−2.990	−2.125	1.30	2.3 ± 0.9	2.05	0.26*
301201	132.7204	+1.2501	0.0348	157.5	8.6/6.5	10.0	$0.57^{+0.02}_{-0.10}$	0.34	−2.673	−2.900	1.42	2.7 ± 0.7	1.37	0.44
594986	222.8160	−0.1633	0.0428	192.5	5.1/4.7	10.2	$0.22^{+0.16}_{-0.15}$	0.36	−2.813	−2.595	1.38	2.3 ± 0.6	1.13	0.22*
623679	139.9831	+0.6413	0.0564	257.2	6.1/7.6	10.2	$1.44^{+0.09}_{-0.40}$	1.02	−2.399	−2.548	1.41	5.4 ± 0.4	2.60	0.25
297667	216.7625	+1.3627	0.0558	253.3	7.5/9.2	10.2	$0.96^{+0.18}_{-0.25}$	1.66	−2.744	−2.507	1.29	4.5 ± 0.4	3.47	0.25
228066	215.8674	+1.1021	0.0397	178.9	5.1/4.4	10.3	$0.26^{+0.08}_{-0.05}$	0.26	−2.678	−2.669	1.74	1.3 ± 0.4	4.19	0.18*
325536	140.9840	+1.8344	0.0507	230.9	6.7/7.4	10.3	$2.07^{+0.36}_{-0.72}$	1.79	−2.224	−2.287	1.36	3.4 ± 0.4	2.33	0.27
496966	212.5919	−1.1150	0.0542	245.8	5.3/6.3	10.4	$1.06^{+0.12}_{-0.07}$	1.31	−2.366	−2.276	1.44	2.9 ± 0.5	3.63	0.22*
348116	140.2934	+2.2012	0.0504	229.4	7.2/8.0	10.6	$0.94^{+0.39}_{-0.20}$	0.64	−2.632	−2.797	1.55	1.2 ± 0.5	1.29	0.42
376293	132.7976	+1.5017	0.0595	271.0	7.0/9.1	10.6	$3.48^{+0.47}_{-0.68}$	2.88	−2.175	−2.257	1.37	3.2 ± 0.4	1.34	0.44
543859	213.1517	−1.0364	0.0538	244.3	7.4/8.8	10.7	$0.86^{+0.46}_{-0.02}$	3.43	−2.747	−2.148	1.47	2.4 ± 0.3	3.98	0.29

This paper has been typeset from a TEX/LATEX file prepared by the author.